arXiv:1405.2302v2 [math-ph] 16 Nov 2014

Mean first passage time for a small rotating trap inside a reflective disk

J. C. Tzou T. Kolokolnikov

Department of Mathematics and Statistics, Dalhousie University, Halifax, Nova Scotia, B3H 3J5 Canada

November 18, 2014

Abstract

We compute the mean first passage time (MFPT) for a Brownian particle inside a two-dimensional disk with reflective boundaries and a small interior trap that is rotating at a constant angular velocity. The inherent symmetry of the problem allows for a detailed analytic study of the situation. For a given angular velocity, we determine the optimal radius of rotation that minimizes the average MFPT over the disk. Several distinct regimes are observed, depending on the ratio between the angular velocity ω and the trap size ε, and several intricate transitions are analyzed using the tools of asymptotic analysis and Fourier series. For $\omega \sim \mathcal{O}(1)$, we compute a critical value $\omega_c > 0$ such that the optimal trap location is at the origin whenever $\omega < \omega_c$, and is off the origin for $\omega > \omega_c$. In the regime $1 \ll \omega \ll \mathcal{O}(\varepsilon^{-1})$ the optimal trap path approaches the boundary of the disk. However as ω is further increased to $\mathcal{O}(\varepsilon^{-1})$, the optimal trap path "jumps" closer to the origin. Finally for $\omega \gg \mathcal{O}(\varepsilon^{-1})$ the optimal trap path subdivides the disk into two regions of equal area. This simple geometry provides a good test case for future studies of MFPT with more complex trap motion.

Key words: mean first passage time, narrow escape, diffusion, moving trap, matched asymptotics, boundary layer

1 Introduction

Numerous problems in nature can be formulated in terms of mean escape time of Brownian particles in the presence of small traps. This is often referred to as the mean first passage time (MFPT) or the narrow escape problem, and there is a large and growing literature on the subject; see for example reviews [1, 2, 3, 4, 5, 6, 7] and references therein. Examples where first-passage problems arise include: oxygen transport in muscle tissue [8], cold atoms in optical traps [9], molecular self-assembly [10], the protein target site location in DNAs [11, 12], signal transduction and immune cell activation [13], search and rescue [14, 15, 5] and predator-prey interactions [16, 17, 15, 18, 19]. See a recent review of the narrow escape problem ([20]) and references therein for more applications and associated methods.

Generally speaking, MFPT problems fall into two classes: either the trap is stationary or it is moving. In the case of a stationary traps, very precise information can be obtained, in particular when the traps have small area [7, 21, 22, 2, 23, 24, 25, 13]. A scenario involving moving traps was introduced in [26] in the context of an annihilation process $A + B \to 0$. While originally motivated by the annihilation of monopole-antimonopole pairs in the early universe, the annihilation reaction may also serve as a model in chemical kinetics and collision-induced quenching of excited-state particles [27, 28]. Subsequent studies [29, 30] have addressed the asymptotics of the long time survival probability of a particle diffusing in a continuum distribution of traps. There is also an extensive literature on searching strategies, where a moving trap represents a searcher (e.g. police) and Brownian particles are sought (e.g. drunken robbers). See for example [16, 31, 17, 18, 32, 19]. In some of this literature, the seeker is assumed to follow some kind of random strategy. For example, in [31] it was shown that an intermittent searching strategy consisting of large jumps and random walks works best under many circumstances where the seeker does not know anything about the target. Other works study pursuit problems where either the seeker or the target have some (or full) information about the other party, and can adjust their strategy accordingly.

In a recent review article of first passage problems in finite domains [33], it is remarked that although problems involving stationary traps have been well-studied, the case of mobile traps still remains largely unexplored. In particular, the only studies to have considered mobile traps in confined geometries have done so in one dimension [34, 35, 36, 37]. Mobile traps are not only more realistic in many applications, but can significantly increase or decrease MFPT depending on parameters of their motion. The goal of this paper is to illustrate these effects in a confined two-dimensional domain.

Let us first briefly review the derivation of the continuum equations for the MFPT as outlined in [1], page 31. We first consider the simplified situation of a particle undergoing a discrete random walk moving in one dimension with a stationary trap located at $x = x_0$. Assume that within Δt time, the particle jumps a distance Δx with equal probability to the left and to the right, and let $v(x)$ denote the mean first passage time of a particle initially located at x. Then the MFPT at location x may be expressed in terms of the MFPT of its two neighboring locations as

$$v(x) = \frac{1}{2}\left\{v(x+\Delta x) + v(x-\Delta x)\right\} + \Delta t\,; \qquad v = 0 \ \text{ at } \ x = x_0\,, \tag{1.1}$$

where the condition $v(x_0) = 0$ indicates that a particle whose starting location coincides with the trap location is expected to survive for precisely zero units of time. Taking the limit $\Delta t, \Delta x \to 0$ and expanding (1.1) in Taylor series, we obtain the continuum equation

$$Dv_{xx} + 1 = 0\,, \quad v(x_0) = 0\,; \qquad D \equiv \frac{(\Delta x)^2}{2\Delta t}\,, \tag{1.2}$$

subject to appropriate boundary conditions. Here, D is the diffusion rate, which can be non-dimensionalized to 1. In Figure 1(a), we illustrate a scenario in which a trap is located at $x = 1/2$ on a domain with reflecting boundaries at $x = 0$ and $x = 1$. The solid curve denotes the MFPT as obtained from a Monte Carlo simulation of 5000 individual agents undergoing an unbiased random walk starting from location $x_i \in (0, 1)$. At each interval of time Δt, each agent takes one step of size Δx to the left or right with equal probability. The quantities are such that $(\Delta x)^2/(2\Delta t) = 1$. An agent that steps outside the domain is reflected back into the domain. The time for each agent to hit the trap is recorded, then averaged over all agents. Repeating the procedure for a set of points on the interval $(0, 1)$, we obtain an approximation for the MFPT as a function of starting location x_i. The dashed curve represents the true MPFT obtained by solving (1.2) with $D = 1$, trap location $x_0 = 1/2$, and pure Neumann boundary conditions $v_x(0) = v_x(1) = 0$. Excellent agreement is observed between the Monte Carlo simulation and the exact solution.

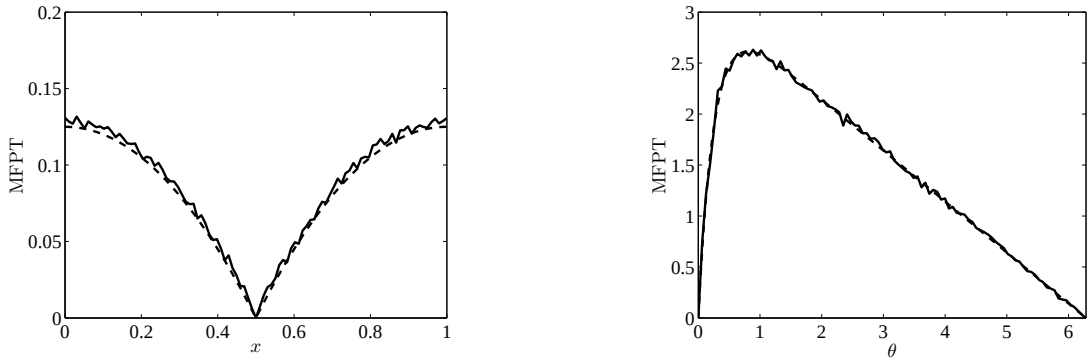

(a) reflecting boundaries (b) periodic boundaries

Figure 1: (a) MFPT on a domain of unit length with reflecting boundaries. The dashed curve is an approximation of the MFPT obtained from a Monte Carlo simulation with $\Delta x = \sqrt{2}/100$ and $\Delta t = 1 \times 10^{-4}$. The diffusion coefficient D defined in (1.2) is then $D = 1$. For each grid point in x, an average of capture times of 5000 agents was used to generate the MFPT. The dashed curve represents the true MPFT obtained by solving (1.2) with $D = 1$ and pure Neumann boundary conditions. (b) MFPT on a one-dimensional circle with trap rotating clockwise at constant angular velocity $\omega > 0$. The plot represents the MFPT for all locations on the circle at the instant when the trap is located at $\theta = 0$. For the Monte Carlo simulation (solid line), $\Delta\theta = 0.01$, $\Delta t = 1 \times 10^{-4}$, and $\omega = 2$. The results are an average over 500 agents at each grid point. The dashed line is the solution of (1.4) with $D = 0.5$ and $\omega = 2$.

A similar derivation may be used to obtain an ODE describing MFPT on a one-dimensional circle $\theta \in [0, 2\pi)$ with a *moving* trap traveling with constant velocity. Consider a trap rotating clockwise on the circle at constant angular velocity $\omega > 0$. At the instant when the trap is located at $\theta = \theta_0$, the MFPT for a particle with initial location θ can be expressed in terms of the MFPT of neighbors of the site equidistant from the trap at the previous time step. Since the trap is displaced by an angle of $-\omega\Delta t$ each time step, we have

$$v(\theta) = \frac{1}{2}\left\{v(\theta + \omega\Delta t - \Delta\theta) + v(\theta + \omega\Delta t + \Delta\theta)\right\} + \Delta t; \qquad v = 0 \text{ at } \theta = \theta_0, \tag{1.3}$$

where we have assumed a jump of $\Delta\theta$ per time step with equal probability in each direction. Expanding (1.3) to leading order, noting that $\mathcal{O}(\Delta\theta) \sim \mathcal{O}(\sqrt{\Delta t})$, we obtain the ODE for MFPT

$$Dv_{\theta\theta} + \omega v_\theta + 1 = 0 \quad v(\theta_0) = 0\,; \qquad D = \frac{(\Delta\theta)^2}{2\Delta t}\,, \tag{1.4}$$

with periodic boundary conditions. The diffusion coefficient in (1.4) may be scaled to unity, leaving a non-dimensional angular velocity in front of the advection term. The Monte Carlo simulation may be performed in the same way as in the case of the stationary trap. On a periodic domain of length 2π, we initialize 500 agents at location $\theta_i \in [0, 2\pi)$ with the trap located at $\theta_0 = 0$. For each time step Δt, we allow each agent to move clockwise or counterclockwise with equal probability, while also advancing the location of the trap by $-\omega\Delta t$, where ω is the speed of the trap. The time required for each agent to be captured is recorded, then averaged over all agents. Repeating the procedure for a discrete set of points on the interval $[0, 2\pi)$, we obtain Figure 1(b). The MFPT in Figure 1(b) therefore represents the MFPT for a random walker starting at location θ at the instant in time when the trap is located at $\theta_0 = 0$. In Figure 1(b), we observe excellent agreement between the solution of (1.4) and a Monte Carlo simulation. The trap is located at $\theta_0 = 0$, and is moving to the left, re-entering at $\theta = 2\pi$ by periodicity. Note that, as expected, the MFPT in front of the rotating trap is lower than that behind the trap.

The mean-field equation (1.4) bears close relation to the parabolic PDE

$$u_t = Du_{\phi\phi} + 1\,, \qquad u(\mathrm{mod}(\omega t, 2\pi), t) = 0\,, \tag{1.5}$$

with periodic boundary boundary conditions and appropriate initial conditions. Applying the transformation $\theta = \phi - \omega t$ and $u(\phi, t) = v(\theta)$ to (1.5), one recovers (1.4) with $\theta_0 = 0$. Note, however, that with $\omega > 0$ in both (1.4) and (1.5), the trap in (1.4) rotates clockwise while it rotates counterclockwise in (1.5). The quantity u in (1.5) is thus different from the MFPT interpretation of v in (1.4). We interpret u as the rescaled continuum limit of a quantity that satisfies the discrete equation

$$u(\phi, t + \Delta t) = \frac{1}{2}\left\{u(\phi + \Delta\phi, t) + u(\phi - \Delta\phi, t)\right\} + r\Delta t\,; \qquad u = 0 \text{ at } \phi = \mathrm{mod}(\omega t, 2\pi)\,. \tag{1.6}$$

A simple interpretation for u in (1.6) is that of a concentration of particles that undergo an unbiased random walk with a constant external feed rate r, which can be normalized to unity. The rotating Dirichlet trap acts to remove particles from the domain. It may also be interpreted as a temperature, with the Dirichlet trap acting to cool a domain subject to uniform external heat influx. For the same set of parameters, the solution for u at a specific instant when the trap is located at $\phi = 2\pi$ is given by Figure 1(b). The trap, however, is to be assumed to be traveling to the right, re-entering at $\phi = 0$. As expected, the concentration or temperature behind the trap is lower than that in front.

In this paper, we examine the MFPT for a moving circular trap of small radius ε inside a unit disk. The trap is assumed to rotate clockwise at a constant rate ω along a circle of radius $r_0 < 1$ concentric with the unit disk. That is, the location of the center of the trap is given by

$$(x_0, y_0) = (r_0 \cos\omega t, -r_0 \sin\omega t)\,. \tag{1.7}$$

The derivation for the elliptic PDE describing the MFPT with this geometry follows closely to that leading to (1.3). That is, for a trap of radius ε centered at (r_0, θ_0) in polar coordinates, the MFPT for a particle initially located at (r, θ) may be expressed in terms of the MFPT of the neighbors of the point $(r, \theta + \omega t)$ at the previous time step. As in the case of the rotating trap on a one-dimensional circle, this equivalence may be attributed the dependence of MFPT on only the relative starting location of the particle with respect to the trap. In Cartesian coordinates, this may be expressed as

$$v(x,y) = \frac{1}{4}\left\{v(x_p+\Delta x, y_p) + v(x_p-\Delta x, y_p) + v(x_p, y_p+\Delta y) + v(x_p, y_p-\Delta y)\right\} + \Delta t\,, \qquad v = 0 \;\text{ when }\; |(x,y)-(x_0,y_0)| \le \varepsilon\,, \tag{1.8}$$

where we have assumed that, at each time step, the particle may move one step on a square lattice with equal probability in all four directions. The condition $v = 0$ when $|(x,y)-(x_0,y_0)| \le \varepsilon$ states that the MFPT of a particle starting inside or on the trap centered at $(x,y) = (x_0,y_0)$ is exactly zero. Since the angular coordinate of the trap location decreases by $\omega\Delta t$ each time step, the location (x_p, y_p) is

$$(x_p, y_p) = (r\cos(\theta+\omega\Delta t), r\sin(\theta+\omega\Delta t))\,. \tag{1.9}$$

Expanding (1.9) for small Δt and using $(x,y) = (r\cos\theta, r\sin\theta)$, we calculate

$$(x_p, y_p) = (x - \omega y\Delta t, y + \omega x\Delta t)\,. \tag{1.10}$$

Substituting (1.10) into (1.8) and expanding to leading order, noting that $\mathcal{O}(\Delta x) \sim \mathcal{O}(\Delta y) \sim \mathcal{O}(\sqrt{\Delta t})$, we obtain

$$\frac{(\Delta x)^2}{4\Delta t}v_{xx} + \frac{(\Delta y)^2}{4\Delta t}v_{yy} + \omega(xv_y - yv_x) + 1 = 0\,, \qquad v = 0 \;\text{ when }\; |(x,y)-(x_0,y_0)| \le \varepsilon\,. \tag{1.11}$$

Letting $\Delta x = \Delta y = \Delta\ell$ and $D \equiv (\Delta\ell)^2/(4\Delta t)$ in (1.11) we obtain in polar coordinates

$$D\Delta v + \omega v_\theta + 1 = 0\,; \qquad v_r(1) = 0\,, \quad v = 0 \;\text{ when }\; |(x,y)-(x_0,y_0)| \le \varepsilon\,, \tag{1.12}$$

where we have used in (1.12) that $xv_y - yv_x = v_\theta$. Both the radius of the disk and the diffusion coefficient D may be scaled to unity without loss of generality. The pure Neumann boundary condition indicates a disk with a reflecting wall. To illustrate the theory, we compare the MFPT obtained from a Monte Carlo simulation (Figure 2(a)) to that of a numerical solution of (1.12) with $D = 1$, $r_0 = 0.6$, $\omega = 200$, and $\varepsilon = 0.1$ (Figure 2(b)). The simulations were performed in the same way as that on the one-dimensional circle, with $\Delta\ell$ and Δt set such that the diffusion coefficient was unity. That is, with a trap of radius ε centered at $(x,y) = (r_0, 0)$, we initialize 1000 agents at a location (x_i, y_i) in the unit disk. We then evolve each agent according to a nearest neighbor random walk, as well as the trap according to (1.7). For each agent, we record the time elapsed before it comes within ε distance of the trap center. The MFPT at point (x_i, y_i) is then approximated by the average capture time of the 1000 particles. Repeating over a grid of points inside the unit disk, we generate Figure 2(a). We observe excellent qualitative agreement between the simulation result and PDE solution. In both figures, the regions with the darkest shade of red have a value of approximately 0.13, indicating also quantitative agreement. Observe that, similar to the case of a rotating trap on a one-dimensional circle, the MFPT is lower in front of the clockwise-rotating trap than it is behind it.

In the same way that the time-independent problem (1.4) may be interpreted as a transformation of the time-dependent problem (1.5) into a rotating frame, the time-dependent analog of (1.12) may be formulated as

$$\begin{aligned} &v_t = \Delta v + 1\,, \quad \mathbf{x} \in \Omega \setminus \Omega_\varepsilon(\mathbf{x}_0(t))\,; \\ \partial_n v = 0\,, \quad \mathbf{x} \in \partial\Omega\,; \qquad &v = 0\,, \quad \mathbf{x} \in \partial\Omega_\varepsilon(\mathbf{x}_0(t))\,; \qquad \mathbf{x}_0(t) = (r_0\cos\omega t, r_0\sin\omega t)\,, \end{aligned} \tag{1.13}$$

supplemented by appropriate initial conditions. Here, $\mathbf{x} = (x,y)$ is a two-dimensional vector in Cartesian coordinates, $v = v(x,y,t)$, Ω denotes the unperturbed unit disk, $\Omega_\varepsilon(\mathbf{x}_0)$ the circular trap of radius ε centered at $\mathbf{x} = \mathbf{x}_0$, and $\partial_n v$ the normal derivative of v on $\partial\Omega$. With $\omega > 0$, the trap rotates counterclockwise. As in (1.6), v may be interpreted as a concentration of particles or a temperature, with the trap acting to remove the quantity from the domain subject to a constant uniform influx. In Figures 2(a) and 2(b), we thus observe the counterclockwise-rotating hole leaving a region of low particle concentration or temperature in its trail.

Our goal is to describe the "optimal" radius $r_0 = r_0^{opt}$ as a function of both ω and ε. For such a rotating trap, we define the optimal radius as the one that minimizes the MFPT *averaged* over all points in the domain. MFPT optimization problems with absorbing boundaries (stationary traps) were considered for particles in one dimension under the presence of a time-oscillatory or randomly fluctuating field in [38, 39, 40, 41, 42, 43]. In these cases, it was found that the average MFPT could be minimized by careful tuning of the characteristics of the field. In contrast, we tune characteristics of the trap motion in order to minimize the average MFPT. In this formulation with the rotating

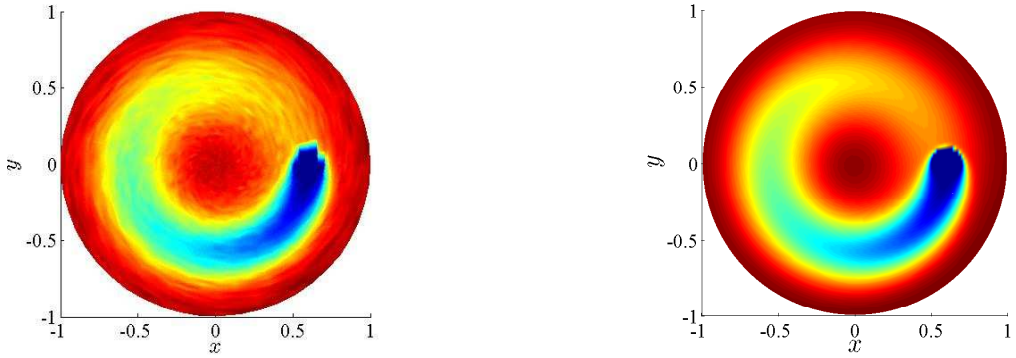

(a) MFPT from Monte Carlo simulation

(b) MFPT from solution of PDE

Figure 2: (a) Monte Carlo approximation of MFPT on a unit disk with trap located at $(x, y) = (0.6, 0)$ rotating clockwise with angular velocity of $\omega = 200$. Red (blue) regions indicate large (small) values of MFPT. The parameters of the random walk are such that $D = 1$. 1000 trials per grid point were used to obtain an average approximation. (b) Numerical solution of (1.12) with $D = 1$ and $\omega = 200$. In both figures, the regions shaded in dark red have a value of approximately 0.13. Observe that the MFPT is lower in front of the trap than it is behind it.

trap, by equivalence between (1.12) with (1.13), minimization of the average MFPT is equivalent to minimizing the total mass

$$M(r_0;\omega) = \int_\Omega v \, d\Omega \,, \tag{1.14}$$

of the solution of (1.13) in the limit $t \to \infty$. We do not consider any transient effects in our analysis. In the rest of this paper, we adopt this interpretation instead of that of the MFPT, as it leads to results and calculations that are more easily interpreted from a physical standpoint.

This is one of the few configurations that is amenable to a full mathematical analysis for a bounded domain in two dimensions. By taking advantage of the radial symmetry, the problem becomes "stationary" in the co-rotating coordinate frame, making it possible to apply a full range of techniques similar to those developed for small stationary traps in [7, 21, 22, 2, 23, 24, 25]. See [20] for a review of asymptotic methods used to study narrow escape problems.

Our main results are summarized in Figure 3. For a range of ω, it shows the optimal radius of rotation r_0^{opt} of the trap that minimizes $M(r_0;\omega)$ with respect to r_0. The analysis shows four distinguished regimes, depending on the relative sizes of ω and ε, as summarized in the following table.

Regime	Main result
$\omega = \mathcal{O}(1)$	"bifurcation" near $\omega = \omega_c$ (§3, §3.1)
$1 \ll \omega \ll \mathcal{O}(\varepsilon^{-1})$	$r_0^{opt} \sim 1$ (§4)
$\omega = \mathcal{O}(\varepsilon^{-1})$	transition region, optimal radius depends only on $\omega_0 = \varepsilon\omega$ (§5)
$\omega \gg \mathcal{O}(\varepsilon^{-1})$.	$r_0^{opt} \sim 1/\sqrt{2}$ (§2)

The left non-zero segment of the solid curve in Figure 3, independent of ε, was generated by calculating $M(r_0;\omega)$ in terms of an infinite series, which may be summed numerically to determine the optimal value of r_0. The analysis, which assumes $\omega \ll \mathcal{O}(\varepsilon^{-1})$, is presented in §3. The circular points are the results of full numerically computed solutions of (1.15) with $\varepsilon = 1 \times 10^{-3}$. A notable feature seen in Figure 3 is the presence of a bifurcation near $\omega_c \approx 3.026$, where for $\omega < \omega_c$, the optimal radius of rotation is precisely 0. This result is due to the optimal location of a stationary trap being at the origin, which we show in §3. The presence of the bifurcation states that a rotating trap must rotate with rate above some critical speed in order to compensate for being located away from this otherwise optimal location. In §3.1, we calculate the critical speed exactly. A typical solution in the regime $\omega \sim \mathcal{O}(1)$ is shown in Figure 4(a) for $\omega = 10$ and $r_0 = 0.6$. Note that solutions for $\omega \sim \mathcal{O}(1)$ lack radial symmetry.

The top dashed line of Figure 3 at $r_0^{opt} = 1$ indicates the value of r_0^{opt} as $\omega \to \infty$ in the regime $1 \ll \omega \ll \mathcal{O}(\varepsilon^{-1})$. In §4 for large ω, we use boundary layers to construct a leading order solution of (1.15). Whereas the analysis of §3

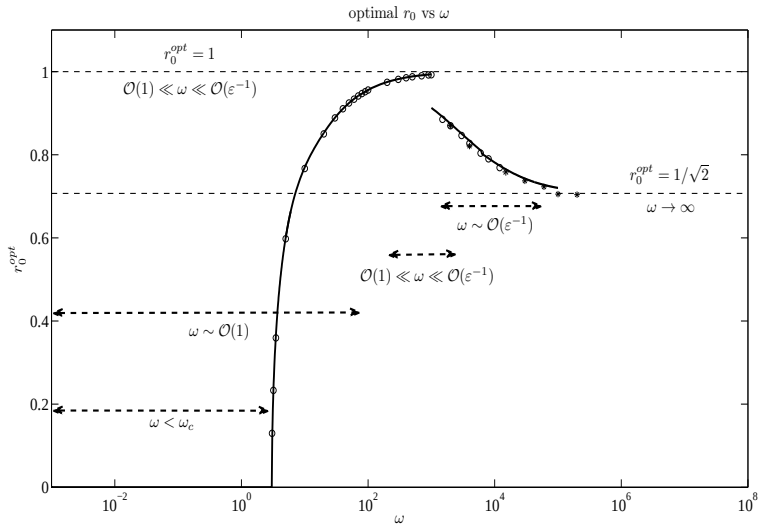

Figure 3: Asymptotic and numerical results for r_0^{opt} in different regimes of ω. Note that the scale of the horizontal axis is logarithmic. The left non-zero segment of the solid curve was obtained from a series solution of (1.15) with $\omega \sim \mathcal{O}(1)$. The top thin dashed line is the result $r_0^{opt} \sim 1$ obtained from a leading order analysis in the regime $1 \ll \omega \ll \mathcal{O}(\varepsilon^{-1})$. The circles were obtained from full numerical solutions of (1.13) with $\varepsilon = 1 \times 10^{-3}$. The right segment of the solid curve was obtained from a leading order calculation with $\omega \sim \mathcal{O}(\varepsilon^{-1})$. The overlaying circles represent results from numerical solutions with $\varepsilon = 1 \times 10^{-3}$. In this regime, the relevant quantity is $\varepsilon\omega$, not ε and ω individually. As such, the stars, generated from the same computations with $\varepsilon = 5 \times 10^{-3}$ and ω one-fifth of the value indicated on the horizontal axis, align closely with the circles. The lower thin dashed line indicates the result $r_0^{opt} \sim 1/\sqrt{2}$ for $\varepsilon \to 0$ and $\omega \to \infty$ with $\omega \gg \mathcal{O}(\varepsilon^{-1})$.

leads to an expression for $M(r_0;\omega)$ in terms of an infinite sum, the boundary layer analysis yields an explicit leading order expression for $M(r_0;\omega)$, from which we readily show that $r_0^{opt} \to 1$ as $\omega \to \infty$ with $\omega \ll \mathcal{O}(\varepsilon^{-1})$. A typical solution in this regime is shown in Figure 4(b). An internal layer develops in the tail behind the trap, while away from this internal layer, the solution is nearly radially symmetric.

The right segment of the solid curve of Figure 3 is calculated from a boundary layer solution with $\omega = \omega_0/\varepsilon$ and $\omega_0 \sim \mathcal{O}(1)$. A very delicate analysis of the boundary layer is required to derive the asymptotic solution. This calculation is presented in §5. Unlike the $\omega \ll \mathcal{O}(\varepsilon^{-1})$ regimes, the results in this regime depend on ε through the quantity $\omega_0 = \varepsilon\omega$. Illustration of this dependence may be seen in Figure 3. While the overlaying circles were determined from numerical solutions with $\varepsilon = 1 \times 10^{-3}$ and ω given on the horizontal axis, the stars were computed with $\varepsilon = 5 \times 10^{-3}$ with ω one-fifth the value on the horizontal axis. The dependence on the product $\varepsilon\omega$ and not on ε and ω individually may be inferred from the close agreement between the circles and stars. A typical solution in this regime is shown in Figure 4(c). Compared to Figure 4(b) with smaller ω, the internal layer in Figure 4(c) is considerably thinner. Away from the layer, the solution also exhibits a high degree of radial symmetry.

Finally, for very large $\omega \gg \mathcal{O}(\varepsilon^{-1})$, the trap is rotating so fast that from the point of view of a particle in the domain, it appears simultaneously everywhere along the circle of radius r_0. In this case the optimal radius asymptotes to $r_0^{opt} \sim 1/\sqrt{2}$. This has a very nice geometric interpretation: the trap moving along such radius divides the unit disk into two regions of equal area. This calculation is presented in §2.

The first step in the analysis is to transform (1.13) into the rotating frame of the trap to obtain a time-independent problem. To do so, we first transform to the polar coordinate system $(x,y) \to (r,\varphi)$ so that $x(r,\varphi) = r\cos\varphi$, $y(r,\varphi) = r\sin\varphi$ and $v(x,y,t) = \tilde{u}(r,\varphi,t)$. The center of the trap is then given by $(r,\varphi) = (r_0, \mathrm{mod}(\omega t, 2\pi))$. Making the transformation into the rotating frame $\theta = \varphi - \mathrm{mod}(\omega t, 2\pi)$ with $0 < \theta < 2\pi$, and $\tilde{u}(r,\varphi,t) = u(r,\theta(t))$, we obtain the stationary problem

$$\Delta u + \omega u_\theta + 1 = 0\,, \quad \mathbf{x} \in \Omega \setminus \Omega_\varepsilon(r_0)\,; \tag{1.15a}$$

$$u_r = 0\,, \quad \mathbf{x} \in \partial\Omega\,; \qquad u = 0\,, \quad \mathbf{x} \in \partial\Omega_\varepsilon(r_0)\,. \tag{1.15b}$$

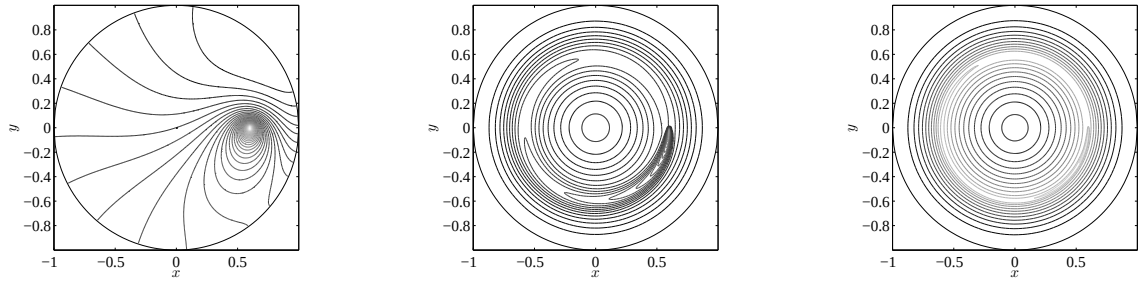

(a) $u(x,y)$ with $\omega = 10$ (b) $u(x,y)$ with $\omega = 1000$ (c) $u(x,y)$ with $\omega = 1 \times 10^4$

Figure 4: Contour plots of $u(x,y)$ obtained by numerically solving (1.15) with $r_0 = 0.6$ and (a) $\omega = 10$, (b) $\omega = 1000$, and (c) $\omega = 1 \times 10^4$. In (a), where $\omega \sim \mathcal{O}(1)$, the solution exhibits no radial symmetry. In (b) for larger ω, an internal layer centered on the ring $r = r_0$ develops behind the trap. The solution is nearly radially symmetric in regions away from the layer. In (c), where $\omega \sim \mathcal{O}(\varepsilon^{-1})$, the layer becomes thinner and the solution exhibits greater radial symmetry. Here, $\varepsilon = 1 \times 10^{-4}$. FlexPDE [44] was used for numerical simulations.

Here, Δu denotes the Laplacian of $u(r,\theta)$ in radial coordinates, u_θ and u_r denote differentiation of u with respect to the angular and radial coordinates, respectively, and $\Omega_\varepsilon(r_0)$ denotes a circular hole of radius ε centered at a distance r_0 from the origin located along the $\theta = 0$ axis.

2 The regime $\omega \gg \mathcal{O}(\varepsilon^{-1})$

This is the simplest regime to analyze, as (1.15) reduces to a radially symmetry problem for u. To see this, we let $\omega \to \infty$ in (1.15a) so that $u = u(r)$ to leading order when $(r,\theta) \neq (r_0, 0)$. In the inner region $\xi = \varepsilon^{-1}(x - x_0)$, $\eta = \varepsilon^{-1} y$, we have for $u = U(\xi,\eta)$ that $\varepsilon^{-2}\Delta U + \varepsilon^{-1}\omega r_0 U_\eta + 1 = 0$, which suggests that $U = U(\xi)$ when $\omega \gg \mathcal{O}(\varepsilon^{-1})$. With $U = 0$ on the trap $|(\xi,\eta)| = 1$, and since it matches to a radially symmetric outer solution, we must have that $U = 0$. In this way, we obtain the limiting outer problem

$$\Delta u + 1 = 0\,, \quad \mathbf{x} \in \Omega \setminus \{\mathbf{x} : r_0 - \varepsilon < |\mathbf{x}| < r_0 + \varepsilon\}\,; \tag{2.1a}$$

$$u_r = 0\,, \quad \mathbf{x} \in \partial\Omega\,; \qquad u \text{ bounded as } r \to 0\,, \quad u = u_0\,, \quad |\mathbf{x}| = r_0 - \varepsilon\,, r_0 + \varepsilon\,, \tag{2.1b}$$

with $u_0 = 0$. The solution of (2.1) with $u_0 = 0$ is

$$u(r) = \frac{r_0^2 + \varepsilon^2 - r^2}{4} + \begin{cases} -\frac{\varepsilon r_0}{2}\,, & 0 < r < r_0 - \varepsilon \\ \frac{\varepsilon r_0}{2} + \frac{1}{2}\log\left(\frac{r}{r_0+\varepsilon}\right)\,, & r_0 + \varepsilon < r < 1 \end{cases}\,. \tag{2.2}$$

In this case, with u given by (2.2), the total mass as defined by (1.14) is

$$M(r_0;\omega) = M(r_0) = \pi\left[\frac{r_0^2}{2} - \frac{3}{8} - \frac{1}{2}\log(r_0 + \varepsilon) + \varepsilon r_0(1 - r_0^2) + \frac{1}{2}\varepsilon^2 - \varepsilon^3 r_0\right]\,. \tag{2.3}$$

The optimal radius of rotation r_0^{opt} that minimizes M satisfies $dM/dr_0 = 0$, yielding

$$r_0^{opt} = \frac{1}{\sqrt{2}} - \frac{\varepsilon}{4} + \mathcal{O}(\varepsilon^2)\,. \tag{2.4}$$

The approach to a value of r_0^{opt} slightly less than $1/\sqrt{2}$ as $\omega \to \infty$ with fixed ε was observed in obtaining the numerical results presented in Figure 3.

For $\varepsilon \to 0$, the optimal radius (2.4) is the same as that obtained in the limit of an analogous problem studied in [25]. The objective of that work was to find configurations for N identical traps placed inside a unit disk that optimized

the fundamental Neumann eigenvalue of the Laplacian. For the special case where the traps were restricted to lie on a ring of radius r, it can be seen from Proposition 4.4 of [25] that the optimal value of r tends to $1/\sqrt{2}$ as $N \to \infty$.

In the following section, we solve (1.15) in the regime $\omega \sim \mathcal{O}(1)$ in terms of a series expansion. Calculating the mass, we find that there exists a value $\omega_c > 0$ independent of ε for which $r_0^{opt} = 0$ when $\omega < \omega_c$ and $0 < r_0^{opt} < 1$ when $\omega > \omega_c$. In §3.1, we use the results of §3 to determine the exact value of ω_c.

3 Asymptotic solution for $\omega \sim \mathcal{O}(1)$

For $\omega = \mathcal{O}(1)$, we solve (1.15) using the method of matched asymptotics as in [25]. Near the trap, we make the change to the inner variables

$$\mathbf{y} = \frac{\mathbf{x} - \mathbf{x}_0}{\varepsilon}\,, \quad u(\mathbf{x}) = U(\mathbf{y})\,; \qquad \mathbf{x}_0 = (r_0, 0)\,, \tag{3.1}$$

so that the trap, in the inner region, is a circle of unit radius denoted Ω_1. Here, $\mathbf{x}_0$ denotes the center of the trap in Cartesian coordinates. With this scaling, we have in the inner region that $\varepsilon^{-2}\Delta U + \varepsilon^{-1}\omega r_0 U_\eta + 1 = 0$. With $\omega \ll \mathcal{O}(\varepsilon^{-1})$, the inner problem for U reduces to

$$\Delta_{\mathbf{y}} U = 0\,, \quad \mathbf{y} \notin \Omega_1\,; \qquad U = 0\,, \quad |\mathbf{y}| = 1\,, \tag{3.2a}$$

$$U \sim S \log|\mathbf{y}| \ \text{ as } \ |\mathbf{y}| \to \infty\,. \tag{3.2b}$$

With $\mathbf{y}$ defined in (3.1), the behavior of u near the trap is determined by the far-field behavior in (3.2b) as

$$u \sim S \log|\mathbf{x} - \mathbf{x}_0| - S \log\varepsilon\,, \ \text{ as } \ \mathbf{x} \to \mathbf{x}_0\,. \tag{3.3}$$

The logarithmic behavior of u as $\mathbf{x} \to \mathbf{x}_0$ suggests that

$$u = -\pi G(\mathbf{x}; \mathbf{x}_0) + H\,, \tag{3.4}$$

where $G(\mathbf{x}; \mathbf{x}_0)$ is the Neumann Green's function satisfying

$$\Delta G + \omega G_\theta = \frac{1}{\pi} - \delta(\mathbf{x} - \mathbf{x}_0)\,, \quad \mathbf{x} \in \Omega\,; \tag{3.5a}$$

$$\partial_r G = 0\,, \quad \mathbf{x} \in \partial\Omega\,; \qquad \int_\Omega G(\mathbf{x}; \mathbf{x}_0)\, d\Omega = 0\,, \tag{3.5b}$$

and H is a constant obtained from matching the inner and outer solutions.

The solution for $G(\mathbf{x}; \mathbf{x}_0)$ in (3.5a) can be written as

$$G(\mathbf{x}; \mathbf{x}_0) = -\frac{1}{2\pi} \log|\mathbf{x} - \mathbf{x}_0| + R(\mathbf{x}; \mathbf{x}_0)\,, \tag{3.6}$$

where $R(\mathbf{x}; \mathbf{x}_0)$ remains finite as $\mathbf{x} \to \mathbf{x}_0$ and is referred to as the regular part of $G(\mathbf{x}; \mathbf{x}_0)$. By (3.4), the behavior of u as $\mathbf{x} \to \mathbf{x}_0$ is then

$$u \sim \frac{1}{2} \log|\mathbf{x} - \mathbf{x}_0| - \pi R(\mathbf{x}_0; \mathbf{x}_0) + H\,, \ \text{ as } \ \mathbf{x} \to \mathbf{x}_0\,. \tag{3.7}$$

Comparing (3.7) to (3.3), we find that $S = 1/2$ and

$$H = \pi R(\mathbf{x}_0; \mathbf{x}_0) - \frac{1}{2} \log\varepsilon\,. \tag{3.8}$$

By (3.4) and (3.5a), we have that the mass of u in Ω is

$$M(r_0; \omega) = \pi H\,, \tag{3.9}$$

with H given in (3.8) and $r_0 = |\mathbf{x}_0|$. The minimization of $M(r_0;\omega)$ is thus equivalent to the minimization of $R(\mathbf{x}_0;\mathbf{x}_0)$. In the case of a stationary trap located at $\mathbf{x} = \mathbf{x}_0$, an explicit formula for the regular part of the Neumann Green's function with $\omega = 0$ in (3.5a) is given in [25] as

$$R_m(\mathbf{x}_0;\mathbf{x}_0) = \frac{1}{2\pi}\left[-\log\left|\mathbf{x}_0|\mathbf{x}_0| - \frac{\mathbf{x}_0}{\mathbf{x}_0}\right| + |\mathbf{x}_0|^2 - \frac{3}{4}\right]. \tag{3.10}$$

With (3.10) for $R(\mathbf{x}_0;\mathbf{x}_0)$ in (3.9), a simply calculation shows that $M(r_0;0)$ is minimized when $r_0 = 0$. We show below that $M(r_0;\omega)$ is minimized at some $0 < r_0 < 1$ when $\omega > \omega_c$, where $\omega_c \approx 3.026$ is an $\mathcal{O}(1)$ constant that we determine in §3.1. When $\omega < \omega_c$ the optimal configuration is a stationary trap located at the origin.

For $\omega > 0$, we now compute $G(\mathbf{x};\mathbf{x}_0)$ in the form of a Fourier series expansion. We first write the equation in (3.5a) in polar coordinates as

$$G_{rr} + \frac{1}{r}G_r + \frac{1}{r^2}G_{\theta\theta} + \omega G_\theta = \frac{1}{\pi} - \frac{1}{r}\delta(r-r_0)\delta(\theta)\,, \tag{3.11}$$

where we have used that the location $\mathbf{x}_0$ of the trap is along the $\theta = 0$ ray. We use separation of variables to write $G(\mathbf{x};\mathbf{x}_0)$ as

$$G(\mathbf{x};\mathbf{x}_0) = G(r,\theta;r_0) = R_0(r) + \sum_{m>0} e^{im\theta}R_m(r) + c.c.\,, \tag{3.12}$$

where $c.c.$ refers to the complex conjugate of the term involving the summation. Substituting (3.12) into (3.11) and recalling the insulating boundary conditions in (3.5b), we obtain

$$R_0'' + \frac{1}{r}R_0' = \frac{1}{\pi} - \frac{1}{2\pi r}\delta(r-r_0)\,, \quad R_0 \text{ bounded as } r\to 0\,, \quad R_0'(1) = 0\,, \tag{3.13a}$$

$$R_m'' + \frac{1}{r}R_m' + \left(i\omega m - \frac{m^2}{r^2}\right)R_m = -\frac{1}{2\pi r}\delta(r-r_0)\,, \quad m>0\,, \quad R_m \text{ bounded as } r\to 0\,, \quad R_m'(1) = 0\,. \tag{3.13b}$$

For $m > 0$, the homogeneous solution of (3.13b) may be written as

$$R_m(r;\omega) = a_m I_m(c_m r) + b_m K_m(c_m r)\,; \qquad c_m \equiv -i\sqrt{i\omega m}\,, \tag{3.14}$$

where $I_m(r)$ and $K_m(r)$ are m-th order modified Bessel functions of the first and second kind, respectively. Solving (3.13b) separately for $r < r_0$ and $r > r_0$, and applying appropriate continuity and jump conditions at $r = r_0$, we obtain the solution for R_m,

$$R_m(r;\omega) = \begin{cases} \frac{1}{2\pi}\left[-\frac{K_m'(c_m)}{I_m'(c_m)}I_m(c_m r_0) + K_m(c_m r_0)\right]I_m(c_m r)\,, & 0<r<r_0 \\ \frac{1}{2\pi}\left[-\frac{K_m'(c_m)}{I_m'(c_m)}I_m(c_m r) + K_m(c_m r)\right]I_m(c_m r_0)\,, & r_0<r<1 \end{cases}, \quad m>0\,, \tag{3.15a}$$

where $I_m'(c_m)$ and $K_m'(c_m)$ denote the derivatives of I_m and K_m evaluated at c_m, respectively. In a similar way, we find that the solution to (3.13a) for $R_0(r)$ is

$$R_0(r) = \frac{r^2}{4\pi} + a_0 - \begin{cases} \frac{1}{2\pi}\log r_0\,, & 0<r<r_0 \\ \frac{1}{2\pi}\log r\,, & r_0<r<1 \end{cases}. \tag{3.15b}$$

Note that the jump condition arising from the right-hand side of (3.13a) is automatically satisfied by (3.15b). The constant a_0 is determined by the zero-mean condition in (3.5b), yielding

$$a_0 = \frac{1}{8\pi}[2r_0^2 - 3]\,. \tag{3.15c}$$

The solution for $G(\mathbf{x};\mathbf{x}_0)$ is then given by (3.12) with (3.15).

To calculate $R(\mathbf{x}_0;\mathbf{x}_0)$, we use (3.6) to write

$$R(\mathbf{x}_0;\mathbf{x}_0) = \lim_{\mathbf{x}\to\mathbf{x}_0}\left\{G(\mathbf{x};\mathbf{x}_0) + \frac{1}{2\pi}\log|\mathbf{x}-\mathbf{x}_0|\right\}. \tag{3.16}$$

We next write $\log|\mathbf{x}-\mathbf{x}_0|$ in terms of its Fourier series as

$$\log|\mathbf{x}-\mathbf{x}_0| = \begin{cases} \log r_0 - \frac{1}{2}\sum_{m>0}\frac{1}{m}\left(\frac{r}{r_0}\right)^m e^{im\theta} + c.c., & r<r_0 \\ \log r - \frac{1}{2}\sum_{m>0}\frac{1}{m}\left(\frac{r_0}{r}\right)^m e^{im\theta} + c.c., & r>r_0 \end{cases}. \tag{3.17}$$

Using the solution for $G(\mathbf{x};\mathbf{x}_0)$ with $\theta\to 0$ and $r\to r_0$ as $\mathbf{x}\to\mathbf{x}_0$, we then use (3.17) to write (3.16) as

$$R(\mathbf{x}_0;\mathbf{x}_0) = \frac{r_0^2}{2\pi} - \frac{3}{8\pi} + \sum_{m>0}\left(R_m(r_0) - \frac{1}{4\pi m}\right) + c.c.. \tag{3.18}$$

Using (3.18), we may then calculate the constant H from (3.8). The solution for u is then given by (3.4) with $G(\mathbf{x};\mathbf{x}_0)$ given by (3.12) with (3.15) and H given by (3.8) and (3.18). A typical solution for u with $\omega = 10$ and $r_0 = 0.6$ is shown in Figure 5(a). The corresponding regular part of u is shown in Figure 5(b). The contour plot of u is shown in Figure 5(c) and agrees with Figure 4(a). Finally, we calculate the mass M in (3.9) as

$$M(r_0;\omega) = \pi\left[\frac{r_0^2}{2} - \frac{3}{8} - \frac{1}{2}\log\varepsilon\right] + \pi^2\sum_{m>0}\left(R_m(r_0;\omega) - \frac{1}{4\pi m}\right) + c.c.. \tag{3.19}$$

Here, $c.c.$ represents the complex conjugate of the term involving the summation, while the parametric dependence of M on ω is through the dependence of R_m on c_m, defined in (3.14).

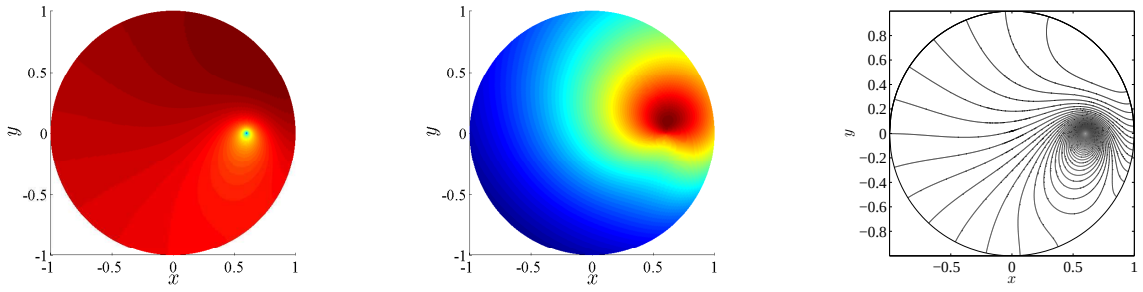

(a) $u(x,y)$ (b) regular part of $u(x,y)$ (c) contour plot of $u(x,y)$

Figure 5: (a) Asymptotic solution $u(x,y)$ of (1.15) with $\omega = 10$, $\varepsilon = 1\times 10^{-4}$, and $r_0 = 0.6$ as constructed from (3.4). (b) The corresponding regular part of $u(x,y)$. Red (blue) regions indicate large (small) values of u. (c) The contour plot of (a); compare with Figure 4(a) for the numerical solution with the same parameters.

For a range of $\omega \ll \mathcal{O}(\varepsilon^{-1})$, we use (3.19) to numerically determine the value of r_0 that minimizes M. The results are presented in Figure 6. The first main feature of Figure 6(a) is the bifurcation that occurs near $\omega = \omega_c \approx 3.026$ (closeup in Figure 6(b)); for $\omega < \omega_c$, the optimal radius of rotation remains zero. In §3.1 below, we expand (3.19) for small $r_0 \ll 1$ to locate the exact value of ω_c at which the bifurcation occurs. The second main feature of Figure 6(a) is the monotonic approach to $r_0^{opt} = 1$ for large ω. In §4, we construct a solution of (1.15) for $1 \ll \omega \ll \mathcal{O}(\varepsilon^{-1})$ to show that $r_0^{opt} \to 1$ as $\omega\to\infty$ with $\omega \ll \mathcal{O}(\varepsilon^{-1})$. Note that this does not conflict with the result in (2.4), as the analysis above, in particular the inner problem (3.2), is valid only when $\omega \ll \mathcal{O}(\varepsilon^{-1})$. The regime $\omega = \mathcal{O}(\varepsilon^{-1})$ is a distinguished limit and is discussed in §5.

3.1 Bifurcation of r_0^{opt} versus ω

The presence of a bifurcation of r_0^{opt} near $\omega = 3$ may be confirmed by obtaining numerical solutions of (1.15). The computations were performed using the FlexPDE finite element PDE solver [44]. In Figure 7, we compare the mass $M(r_0;\omega)$ as given by (3.19) with that computed from numerical solutions of (1.15). In Figure 7(a), we show that

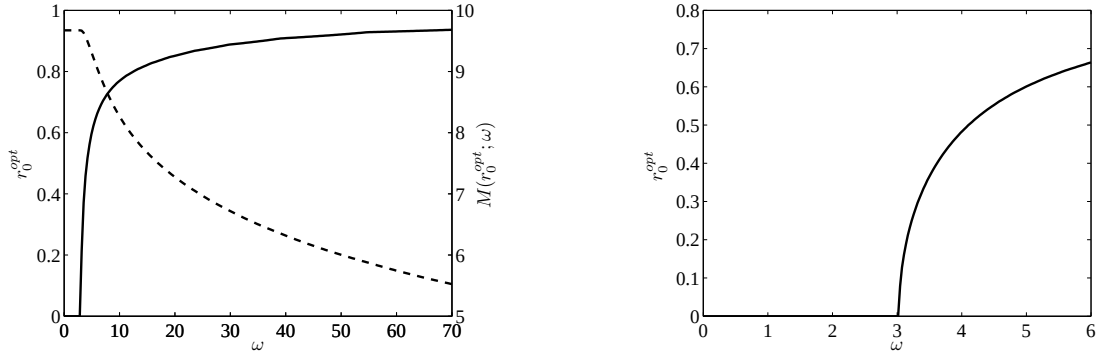

(a) r_0^{opt} versus ω (b) r_0^{opt} versus ω near bifurcation point

Figure 6: (a) Plot of r_0^{opt} versus $\omega \ll \mathcal{O}(\varepsilon^{-1})$ (solid, left vertical axis) and the corresponding mass $M(r_0^{opt};\omega)$ (dashed, right vertical axis). The optimal radius remains zero for ω sufficiently small. (b) Closeup of the bifurcation point near $\omega \approx 3$ past which the optimal radius becomes non-zero.

when $\omega = 2$, the concavity at the point $r_0 = 0$ is positive with $M(r_0;\omega)$ increasing on the entire interval $0 < r_0 < 1$, yielding $r_0^{opt} = 0$. In Figures 7(b) and 7(c) with $\omega = 3.5$, we show that the concavity at $r_0 = 0$ has become negative, thereby yielding $r_0^{opt} > 0$. The bifurcation seen in Figure 6(b) must then occur when the quadratic behavior of $M(r_0;\omega)$ near $r_0 = 0$ changes from concave up to concave down. We may thus determine the bifurcation point by expanding $M(r_0;\omega)$ in (3.19) in powers of r_0 and calculating the value of ω at which the coefficient of r_0^2 changes sign. In the following analysis, we assume that $r_0 \gg \mathcal{O}(\varepsilon)$.

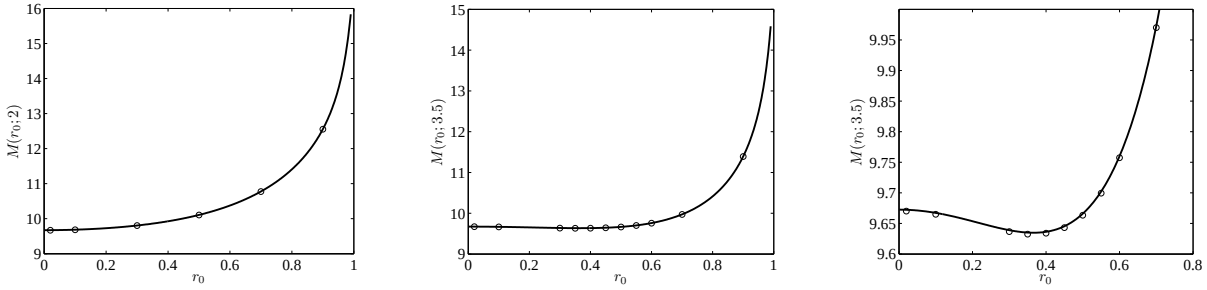

(a) $M(r_0)$ for $\omega = 2$ (b) $M(r_0)$ for $\omega = 3.5$ (c) $M(r_0)$ for $\omega = 3.5$ closeup

Figure 7: Plots of $M(r;\omega)$ for (a) $\omega = 2$ and (b),(c) $\omega = 3.5$. The solid curves are calculated from (3.19), while the circles are obtained from numerical solutions of (1.15). In (a) with $\omega = 2$, the point $r_0 = 0$ is a global minimum so that $r_0^{opt} = 0$, while in (b) with $\omega = 3.5$, it is a local maximum (closeup in (c)), yielding $r_0^{opt} > 0$. Here, $\varepsilon = 1 \times 10^{-3}$.

To simplify calculations, we equivalently seek the leading order term of the expansion in r_0 of the quantity

$$S = \frac{r_0^2}{2} - 2\Re\left\{\sum_{m>0}\left(-\pi R_m(r_0;\omega) + \frac{1}{4m}\right)\right\}, \tag{3.20}$$

where $R_m(r;\omega)$ is given in (3.15a). To do so, we write the ascending series representation of $I_\nu(z)$ and $K_\nu(z)$ for $\nu > 0$ given in [45] as

$$I_\nu(z) = \left(\frac{z}{2}\right)^\nu \sum_{k=0}^{\infty} \frac{(z^2/4)^k}{k!\Gamma(\nu+k+1)}, \tag{3.21a}$$

$$K_\nu(z) = \frac{1}{2}\left(\frac{z}{2}\right)^{-\nu}\sum_{k=0}^{\nu-1}\frac{(n-k-1)!}{k!}\left(-\frac{z^2}{4}\right)^k + (-1)^{\nu+1}\log\left(\frac{z}{2}\right)I_\nu(z)$$
$$+ (-1)^\nu\frac{1}{2}\left(\frac{z}{2}\right)^\nu\sum_{k=0}^{\infty}\left[\psi(k+1)+\psi(\nu+k+1)\right]\frac{(z^2/4)^k}{k!(n+k)!}\,, \quad (3.21b)$$

where γ is Euler's constant, and $\psi(n)$ is given by

$$\psi(n) = \begin{cases} -\gamma\,, & n=1 \\ -\gamma+\sum_{k=1}^{n-1}\frac{1}{k}\,, & n>1 \end{cases}\,. \quad (3.21c)$$

With (3.21) and (3.15a), we find that

$$-\pi R_1(r_0;\omega) \sim -\frac{1}{4}+\frac{c_1^2}{8}\left[-\frac{1}{4}-\log\left(\frac{c_1 r_0}{2}\right)+\frac{K_1'(c_1)}{I_1'(c_1)}+\frac{1}{2}(1-2\gamma)\right]r_0^2\,; \qquad c_1\equiv -i\sqrt{i\omega} \quad (3.22a)$$

$$-\pi R_m(r_0;\omega) \sim -\frac{1}{4m}+\frac{c_m^2}{8m(m^2-1)}r_0^2\,; \qquad m>1\,, \quad c_m\equiv -i\sqrt{i\omega m}\,. \quad (3.22b)$$

The $(4m)^{-1}$ term in (3.20) cancels the leading order constant term in (3.22a) and (3.22b). Further, since c_m^2 is pure imaginary, only the $m=1$ term contributes to the leading order quadratic behavior of S. We therefore have, for $\varepsilon \ll r_0 \ll 1$,

$$S \sim a_2(\omega) r_0^2; \qquad a_2(\omega) \equiv \frac{1}{2} - 2\Re\left\{\frac{c_1^2}{8}\left[-\frac{1}{4}-\log\left(\frac{c_1 r_0}{2}\right)+\frac{K_1'(c_1)}{I_1'(c_1)}+\frac{1}{2}(1-2\gamma)\right]\right\}\,, \quad (3.23)$$

where the dependence of $a_2(\omega)$ on ω is through c_1 defined in (3.22a). The value $\omega=\omega_c$ at which the concavity of S at $r_0=0$ changes sign is the value at which the optimality of $r_0=0$ is lost. The bifurcation point therefore must satisfy

$$a_2(\omega_c) = 0\,, \quad (3.24)$$

where $a_2(\omega)$ is defined in (3.23). Solving (3.24) numerically for ω_c, we find that the bifurcation in Figure 6(b) occurs at $\omega_c \approx 3.026$.

4 Leading order solution for large ω with $\omega \ll \mathcal{O}(\varepsilon^{-1})$

As ω in (1.15a) becomes large with $\omega \ll \mathcal{O}(\varepsilon^{-1})$, an internal layer of width $\mathcal{O}(\omega^{-1/2})$ develops in a trail behind the rotating trap. An example of this is shown in Figure 4(b), obtained by numerically solving (1.15) with $\omega=1000$ and $\varepsilon = 1\times 10^{-4}$. An asymptotic solution with the same parameters is shown in Figure 8(a). The internal layer centered on the ring $r=r_0$ may be clearly seen in the corresponding contour plot in Figure 8(b). Away from the internal layer, the solution is nearly radially symmetric. We now construct this solution and derive an approximation to the mass $M(r_0;\omega)$ in (3.19) for large ω. We then show that as $\omega\to\infty$ with $\omega \ll \mathcal{O}(\varepsilon^{-1})$, the optimal radius $r_0^{opt}\to 1$. The analysis below assumes that $1-r_0\sim\mathcal{O}(1)$ and $r_0\omega \gg 1$.

To construct a solution of (1.15a), we first identify three distinct regions of the solution of (3.5a). In addition to the $\mathcal{O}(\varepsilon)$ region identified in (3.2) and the $\mathcal{O}(\omega^{-1/2})$ internal parabolic layer seen in Figure 8(b), there is an elliptic layer of extent $\mathcal{O}(\omega^{-1})$ surrounding the $\mathcal{O}(\varepsilon)$ region. The solution will be constructed by matching the elliptic layer to the $\mathcal{O}(\varepsilon)$ inner region, and then the parabolic layer to the elliptic layer.

For the elliptic layer, the Cartesian coordinate system is convenient. In the $\mathcal{O}(\omega^{-1})$ vicinity of the trap, we make the change of variables

$$\xi = \omega(x-r_0)\,, \quad \eta=\omega y\,; \qquad G(r,\theta)=\hat{G}(\xi,\eta)\,. \quad (4.1)$$

Substituting (4.1) into (3.11) with $G_\theta = xG_y - yG_x$ and using the scaling property of the delta function $\delta(ax)=\delta(x)/|a|$, the leading order equation for $\omega\gg 1$ becomes

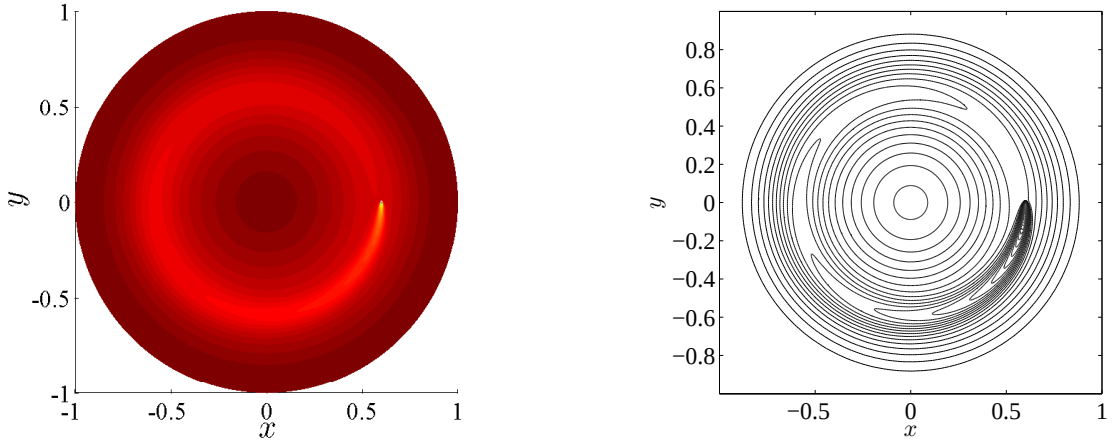

(a) $u(x,y)$ (b) contour plot of $u(x,y)$

Figure 8: (a) Asymptotic solution $u(x,y)$ of (1.15) with $\omega = 1000 \gg 1$, $\varepsilon = 1 \times 10^{-4}$, and $r_0 = 0.6$ as constructed from (3.4). Red (blue) regions indicate large (small) values of u. (b) The corresponding contour plot of $u(x,y)$. An internal layer of width $\mathcal{O}(\omega^{-1/2})$ centered on the ring $r = r_0$ is clearly seen. The solution is nearly radially symmetric away from the internal layer. Compare with Figure 4(b) for the numerical solution with the same parameters.

$$\hat{G}_{\xi\xi} + \hat{G}_{\eta\eta} + r_0\hat{G}_\eta = -\delta(\xi)\delta(\eta)\,; \qquad -\infty < \xi\,, \eta < \infty\,, \quad \hat{G} \text{ bounded as } |\xi|\,, |\eta| \to \infty\,. \tag{4.2}$$

The condition at infinity in (4.2) is required to match the elliptic intermediate layer to the parabolic internal layer. To solve (4.2), we proceed as in [46] and write

$$\hat{G}(\xi,\eta) = \mathcal{G}(\rho)e^{-\frac{r_0}{2}\eta} + \hat{H}\,; \qquad \rho^2 = \xi^2 + \eta^2\,, \quad -\infty < \xi\,, \eta < \infty\,, \quad 0 < \rho < \infty\,, \tag{4.3}$$

where $\hat{H}$ is a constant to be determined from the zero mean-condition in (3.5b). Substituting (4.3) into (4.2), we calculate

$$\mathcal{G}_{\rho\rho} + \frac{1}{\rho}\mathcal{G}_\rho - \left(\frac{r_0}{2}\right)^2 \mathcal{G} = -\frac{1}{2\pi\rho}\delta(\rho)\,; \qquad 0 < \rho < \infty\,, \tag{4.4a}$$

$$\mathcal{G} \text{ bounded as } \rho \to \infty\,. \tag{4.4b}$$

The homogeneous solution of (4.4a) is given by a linear combination of modified Bessel functions

$$\mathcal{G}(\rho) = c_1 I_0\left(\frac{r_0\rho}{2}\right) + c_2 K_0\left(\frac{r_0\rho}{2}\right)\,. \tag{4.5}$$

In (4.5), $c_1 = 0$ by the boundedness condition in (4.4b), while c_2 is determined by integrating (4.4a) over a circle of radius $\delta \to 0$,

$$\lim_{\delta\to 0} 2\pi\delta c_2 \frac{d}{d\rho} K_0\left(\frac{r_0\rho}{2}\right)\Big|_{\rho=\delta} = -1\,. \tag{4.6}$$

Using the small argument asymptotics for $K_0(z)$,

$$K_0(z) \sim -\log\frac{z}{2} - \gamma\,, \tag{4.7}$$

we calculate from (4.6) that $c_2 = (2\pi)^{-1}$ in (4.5). The solution of (4.2) for the elliptic layer is then given by

$$\hat{G}(\xi,\eta) = \frac{1}{2\pi} K_0\left(\frac{r_0}{2}\sqrt{\xi^2+\eta^2}\right) e^{-\frac{r_0}{2}\eta} + \hat{H}\,, \tag{4.8}$$

where $\hat{H}$ is a constant to be computed, while ξ and η are defined in (4.1).

For the parabolic layer of thickness $\mathcal{O}(\omega^{-1/2})$, we introduce the scaled variables

$$\tilde{\theta} = 2\pi - \theta\,, \quad \tilde{r} = \sqrt{\omega}(r - r_0)\,; \qquad G(r,\theta) = \tilde{G}(\tilde{r},\tilde{\theta})\,. \tag{4.9}$$

Substituting (4.9) into (3.11) and collecting terms of $\mathcal{O}(\omega)$, we obtain the parabolic equation

$$\tilde{G}_{\tilde{\theta}} = \tilde{G}_{\tilde{r}\tilde{r}}\,; \qquad 0 < \tilde{\theta} < 2\pi\,, \quad -\infty < \tilde{r} < \infty\,. \tag{4.10}$$

We require boundedness of $\tilde{G}$ as $|\tilde{r}| \to \infty$ in order to match to the outer region. We now compute a solution of (4.10) that matches the behavior of the elliptic layer (4.8) as $\eta \to -\infty$. To do so, we first use the large argument asymptotic form $K_0(z) \sim \sqrt{\frac{\pi}{2z}} e^{-z}$ as $z \to \infty$, to calculate

$$\hat{G}(\xi,\eta) \sim \frac{1}{\sqrt{4\pi r_0|\eta|}}\, e^{-\frac{r_0\xi^2}{4|\eta|}} + \hat{H}\,, \qquad \eta \to -\infty\,. \tag{4.11}$$

To write ξ and η in terms of $\tilde{r}$ and $\tilde{\theta}$, we first note that, near $r = r_0$ and $\tilde{\theta} = 0^+$, we have that $x \sim r_0 + \tilde{r}$ and $y \sim -r_0\tilde{\theta}$. With ξ and η defined in (4.1), we obtain

$$\xi \sim \sqrt{\omega}\tilde{r}\,, \quad \eta \sim -\omega r_0 \tilde{\theta}\,; \qquad \tilde{\theta} > 0\,. \tag{4.12}$$

Substituting (4.12) into (4.11), we obtain the solution for the parabolic layer

$$\tilde{G}(\tilde{r},\tilde{\theta}) = \frac{1}{2r_0\sqrt{\pi\omega\tilde{\theta}}}\, e^{-\frac{\tilde{r}^2}{4\tilde{\theta}}} + \hat{H}\,. \tag{4.13}$$

The solution (4.13) may also be obtained in a similar way by explicitly calculating the initial condition for (4.10) in terms of a weighted delta function

$$\tilde{G}(\tilde{r},0) = \frac{1}{r_0\sqrt{\omega}}\delta(\tilde{r}) + \hat{H}\,. \tag{4.14}$$

The solution to (4.10) with initial conditions given by (4.14) may then be written in terms of the fundamental solution of the diffusion equation, yielding (4.13).

With (4.8) and (4.13), the inner solution for G in (3.11) near the ring $r = r_0$ is then given by the composite solution $G_i(r,\theta) = \hat{G} + \tilde{G} - c_p$, where c_p is the common part given by (4.11). We thus calculate

$$G_i(r,\theta) = \frac{1}{2\pi} K_0\left(\frac{r_0}{2}\sqrt{\xi^2+\eta^2}\right) e^{-\frac{r_0}{2}\eta} + \frac{1}{2r_0\sqrt{\pi\omega(2\pi-\theta)}} e^{-\frac{\omega(r-r_0)^2}{4(2\pi-\theta)}} - \frac{1}{2\sqrt{\pi r_0|\eta|}}\, e^{-\frac{r_0\xi^2}{4|\eta|}}\Theta(-\eta) + \hat{H}\,, \tag{4.15}$$

where $\xi = \xi(r,\theta)$ and $\eta = \eta(r,\theta)$ are defined in (4.1). For the outer solution G_0 of (3.11), we note that, to leading order in ω, $G_{0\theta} = 0$. For $G_0 = G_0(r)$ radially symmetric, we integrate both sides of (3.11) from $\theta : 0 \to 2\pi$ to obtain

$$G_{0rr} + \frac{1}{r}G_{0r} = \frac{1}{\pi} - \frac{1}{2\pi r}\delta(r - r_0)\,; \qquad 0 < r < 1\,, \quad G_{0r}(1) = 0\,. \tag{4.16a}$$

A unique solution of (4.16a) may be obtained by imposing the matching condition

$$G_0(r_0) = \hat{H}\,, \tag{4.16b}$$

obtained from letting $\omega \to \infty$ in (4.15) with $|r - r_0|$ remaining of $\mathcal{O}(1)$. The solution of (4.16) is then

$$G_0(r) = \frac{r^2 - r_0^2}{4\pi} - \frac{1}{2\pi}\Theta(r - r_0)\log\left(\frac{r}{r_0}\right) + \hat{H}\,, \tag{4.17}$$

where $\Theta(r)$ is the Heaviside step function. The leading order composite solution of (3.11) for $\omega \gg 1$ is then given by $G = G_0 + G_i - \hat{H}$, yielding

$$G(r,\theta) = \frac{r^2 - r_0^2}{4\pi} - \frac{1}{2\pi}\Theta(r-r_0)\log\left(\frac{r}{r_0}\right) + \frac{1}{2\pi}K_0\left(\frac{r_0}{2}\sqrt{\xi^2+\eta^2}\right)e^{-\frac{r_0}{2}\eta} + \\ + \frac{1}{2r_0\sqrt{\pi\omega(2\pi-\theta)}}e^{-\frac{\omega(r-r_0)^2}{4(2\pi-\theta)}} - \frac{1}{2\sqrt{\pi r_0|\eta|}}e^{-\frac{r_0\xi^2}{4|\eta|}}\Theta(-\eta) + \hat{H} + \mathcal{O}(\omega^{-1})\,, \quad (4.18a)$$

where we have used (4.15) and (4.17) for G_i and G_0. The constant $\hat{H}$ is determined by the zero-mean condition in (3.5b). Since the solution in (4.18a) omits terms of order $\mathcal{O}(\omega^{-1})$, and with inner layer terms contributing a mean of $\mathcal{O}(\omega^{-1})$, we need only account for the mean of the first two terms in (4.18a). That is,

$$\hat{H} = -\frac{1}{\pi}\left[-\frac{r_0^2}{2} + \frac{3}{8} + \frac{1}{2}\log r_0\right] + \mathcal{O}(\omega^{-1})\,. \quad (4.18b)$$

The solution to u is then given by (3.4) with G and $\hat{H}$ defined in (4.18).

We now calculate the constant H in (3.4) by the matching condition given in (3.3) with $S = 1/2$. To determine the asymptotic behavior of G as $\mathbf{x} \to \mathbf{x}_0$, we first note that the second and third terms in (4.15), by construction, cancel near the trap, while $G_0(r) \to \hat{H}$. Therefore, using the small argument asymptotics for $K_0(z)$ in (4.7), we calculate that

$$G \sim \frac{1}{2\pi}\left[-\log|\mathbf{x}-\mathbf{x}_0| - \log\left(\frac{r_0\omega}{4}\right) - \gamma\right] + \hat{H}\,, \quad \text{as } \mathbf{x} \to \mathbf{x}_0\,, \quad (4.19)$$

where we have used (4.1) to write ξ and η in terms of x and y. With the asymptotics for G in (4.19), (3.3) and (3.4) yield the matching condition at the trap

$$\frac{1}{2}\left[\log|\mathbf{x}-\mathbf{x}_0| + \log\left(\frac{r_0\omega}{4}\right) + \gamma\right] - \pi\hat{H} + H \sim \frac{1}{2}\log|\mathbf{x}-\mathbf{x}_0| - \frac{1}{2}\log\varepsilon\,. \quad (4.20)$$

Solving for H in (4.20), we obtain

$$H = \pi\hat{H} - \frac{1}{2}\left[\log\left(\frac{r_0\omega\varepsilon}{4}\right) + \gamma\right]\,. \quad (4.21)$$

In Figures 9(a) and 9(b), we show a solution constructed with G and H as given in (4.18) and (4.21). The parameters are the same as those used in Figures 4(b) and 8. In Figure 9(c), we show the corresponding value of u along the ring $r = r_0$. The solid curve is computed numerically from the series expansion of §2, while the dashed curve is computed from the asymptotic construction (4.18) and (4.21). The figure indicates excellent agreement between the two results.

Finally, with H given in (4.21) and $\hat{H}$ defined by (4.18b), we use (3.9) to calculate the mass

$$M(r_0;\omega) = \pi\left[\frac{r_0^2}{2} - \log r_0 - \frac{3}{8} - \frac{1}{2}\log\left(\frac{\varepsilon\omega}{4}\right) - \frac{\gamma}{2}\right] + \mathcal{O}(\omega^{-1})\,, \quad (4.22)$$

valid for $r_0\omega \gg 1$. Differentiating (4.22) by r_0, we find that $r_0^{opt} = 1$ as $\omega \to \infty$ with $\omega \ll \mathcal{O}(\varepsilon^{-1})$, consistent with the results of Figure 3. In Figure 10 for $\omega = 1000$ and $\varepsilon = 1 \times 10^{-4}$, we show a plot of the total mass as computed by (3.19) (solid) and (4.22) (dashed). The circles are data from full numerical solutions of (1.15). In the case of the former, the optimal value of r_0 is slightly less than one, while the latter case indicates that $r_0 = 1$ is optimal. The discrepancy is likely due to the $\mathcal{O}(\omega^{-1})$ terms neglected in (4.22), and violation of the assumption $1 - r_0 \sim \mathcal{O}(1)$.

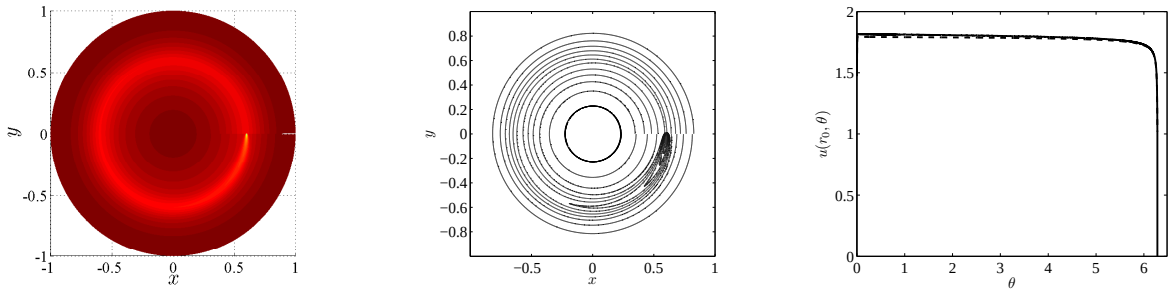

(a) $u(x,y)$ (b) contour plot of $u(x,y)$ (c) value of u on $r = r_0$

Figure 9: (a) Leading order asymptotic solution $u(x,y)$ of (1.15) with $\omega = 1000$, $\varepsilon = 1 \times 10^{-4}$, and $r_0 = 0.6$ as constructed from (4.18) and (4.21). The parameters are the same as those used in Figures 4(b) and 8. Red (blue) regions indicate large (small) values of u. (b) The corresponding contour plot of $u(x,y)$. (c) The value of u along the ring $r = r_0$. The solid curve is computed numerically from the series expansion, while the dashed curve is computed from (4.18) and (4.21).

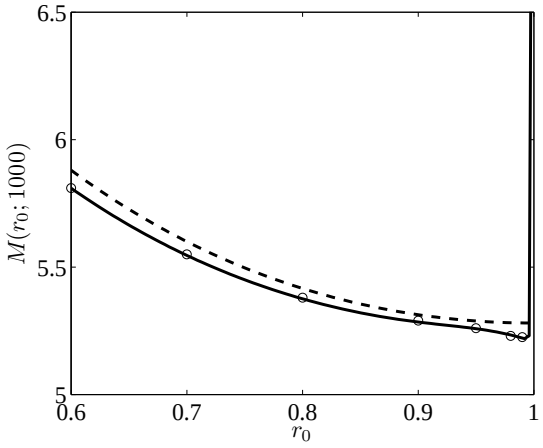

Figure 10: Total mass versus r_0 as computed from (3.19) (solid), (4.22) (dashed), and the full numerical solution of (1.15) (circles). The discrepancy near $r_0 = 1$ is likely due to the $\mathcal{O}(\omega^{-1})$ terms neglected in (4.22) and violation of the assumption $1 - r_0 \sim \mathcal{O}(1)$. Here, $\omega = 1000$ and $\varepsilon = 1 \times 10^{-4}$.

5 The regime $\omega \sim \mathcal{O}(\varepsilon^{-1})$

In Figure 3, we observe a transition from $r_0^{opt} \sim 1$ to $r_0^{opt} \sim 1/\sqrt{2}$ in the regime $\omega = \mathcal{O}(\varepsilon^{-1})$. In this section, we analyze this transition. Unlike the analysis of §4 in which we constructed an explicit solution for u in the inner region, here we employ a boundary integral method to extract only the essential information required to determine the optimal radius of rotation. We first note from §4 that the elliptic layer of extent $\mathcal{O}(\omega^{-1})$ coincides with the inner layer of extent $\mathcal{O}(\varepsilon)$ when $\omega \sim \mathcal{O}(\varepsilon^{-1})$. The regime $\omega \sim \mathcal{O}(\varepsilon^{-1})$ is thus a distinguished regime not contained in the analysis of §§3 or 4. Indeed, with $\omega = \varepsilon^{-1}\omega_0$ with $\omega_0 = \mathcal{O}(1)$, the inner equation for (1.15) becomes the radially asymmetric problem

$$u_{\xi\xi} + u_{\eta\eta} + \omega_0 r_0 u_\eta = 0\,, \quad (\xi,\eta) \notin \Omega_1\,, \qquad u = 0\,, \quad (\xi,\eta) \in \partial\Omega_1\,, \qquad u \sim u_0(s_0) \ \text{ as } \ |(\xi,\eta)| \to \infty\,. \tag{5.1}$$

Here, $(\xi,\eta) = \varepsilon^{-1}(x - x_0, y)$ and $\partial\Omega_1$ is the unit circle. Our goal is to compute the value of $u_0(s_0)$, which determines the value of u on the ring $r = r_0$ in the outer problem. To do so, we first let $u = u_0\mu(\xi,\eta) + u_0$ in (5.1) so that we have

$$\Delta\mu + s_0\mu_\eta = 0\,, \quad (\xi,\eta) \notin \Omega_1\,, \qquad \mu = -1\,, \quad \boldsymbol{\xi} \in \partial\Omega_1\,, \qquad \mu \sim 0 \ \text{ as } \ |\boldsymbol{\xi}| \to \infty\,; \quad s_0 \equiv r_0\omega_0\,. \tag{5.2}$$

In (5.2), $\boldsymbol{\xi} = (\xi,\eta)$ and Δ denotes the Laplacian with respect to the $\boldsymbol{\xi}$. To calculate $u_0(s_0)$, we use a boundary integral method to reformulate (5.2) as an integral equation for the normal derivative $\partial\mu/\partial n$ on $\partial\Omega_1$ (the same approach for solving (5.2) with different a geometry is adopted in [47] in the context of diffusion in the presence of steady two-dimensional potential flow around a finite absorber). The constant $u_0(s_0)$ is then calculated by integrating (1.15) over Ω and imposing the solvability condition that the flux on $\partial\Omega_1$ must be equal to $-\pi$. That is, $u_0(s_0)$ is given by

$$u_0(s_0) = \frac{-\pi}{\Phi(s_0)}\,; \qquad \Phi(s_0) \equiv \int_{\partial\Omega_1} \frac{\partial\mu}{\partial n}\, dS\,. \tag{5.3}$$

The dependence of u_0 on s_0 is due to the appearance of s_0 as a parameter in the equation for μ in (5.2).

We first consider the Green's function for the adjoint problem

$$\Delta\tilde{G} - s_0\tilde{G}_\eta = \delta(\boldsymbol{\xi} - \mathbf{z})\,, \quad \tilde{G} \to 0 \ \text{ as } \ |\boldsymbol{\xi}| \to \infty\,; \qquad \mathbf{z} = (z_1, z_2)\,. \tag{5.4}$$

The solution of (5.4) is given by

$$\tilde{G}(\boldsymbol{\xi};\mathbf{z}) = -\frac{1}{2\pi} e^{\frac{s_0}{2}(\eta - z_2)} K_0\left(\frac{s_0}{2}|\boldsymbol{\xi} - \mathbf{z}|\right)\,. \tag{5.5}$$

Next, we multiply (5.2) by $\tilde{G}$, integrate by parts, use Green's second identity, and apply the boundary conditions to obtain that

$$\mu(\rho\cos\phi, \rho\sin\phi) = \int_0^{2\pi} \frac{\partial\tilde{G}}{\partial\tilde{r}}\bigg|_{\tilde{r}=1} d\tilde{\theta} + \int_0^{2\pi} \left(\tilde{G}\,\frac{\partial\mu}{\partial\tilde{r}}\right)_{\tilde{r}=1} d\tilde{\theta} - s_0 \int_0^{2\pi} \tilde{G}\,\Big|_{\tilde{r}=1} \sin\tilde{\theta}\, d\tilde{\theta}\,. \tag{5.6}$$

In (5.6), we have made the substitutions $(\xi,\eta) \to (\tilde{r}\cos\tilde{\theta}, \tilde{r}\sin\tilde{\theta})$ and $(z_1, z_2) \to (\rho\cos\phi, \rho\sin\phi)$. To obtain an integral equation for $\sigma(\tilde{\theta}) \equiv \partial\mu/\partial\tilde{r}$ on $\partial\Omega_1$, we impose the condition in (5.2) that $\mu = -1$ on $(\rho,\phi) = (1,\phi)$ for $\phi \in [0, 2\pi)$. Imposing this condition in (5.6), we obtain the integral equation for $\sigma(\tilde{\theta})$

$$-\int_0^{2\pi} \tilde{G}\Big|_{\tilde{r}=\rho=1} \sigma(\tilde{\theta})\, d\tilde{\theta} = \frac{1}{2} + \int_0^{2\pi} \frac{\partial\tilde{G}}{\partial\tilde{r}}\bigg|_{\tilde{r}=\rho=1} d\tilde{\theta} - s_0 \int_0^{2\pi} \tilde{G}\,\Big|_{\tilde{r}=\rho=1} \sin\tilde{\theta}\, d\tilde{\theta}\,; \qquad \sigma(\tilde{\theta}) \equiv \frac{\partial\mu}{\partial\tilde{r}}\bigg|_{\tilde{r}=1}\,. \tag{5.7}$$

The $1/2$ term on the right-hand side of (5.7) is a result of evaluating μ on the boundary Ω_1 and thus integrating over only half of the delta function in its Green's function representation. For a range of s_0, we finally solve (5.7) as a linear system for $\sigma(\tilde{\theta})$ at discrete values of $\tilde{\theta}$ and use (5.3) to calculate $u_0(s_0)$. The results of this calculation are shown in Figure 11(a), where we show both u_0 (solid) and u_0' (dashed).

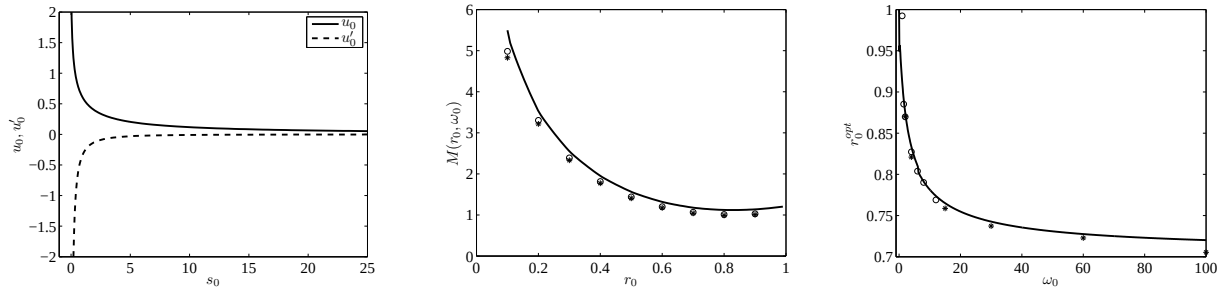

(a) u_0 and u_0' (b) mass versus r_0 with $\omega_0 = 4$ (c) r_0^{opt} versus ω_0

Figure 11: (a) Numerically computed values of $u_0(s_0)$ and $u_0'(s_0)$ for a range of s_0. Here, s_0 is defined in (5.2). (b) Comparison of $M(r_0;\omega)$ as given by (5.11) with $\omega_0 = 4$ (solid curve) and the numerical solution of (1.15) with $\varepsilon = 2.5 \times 10^{-3}$, $\omega = 1600$ (circles) and $\varepsilon = 5 \times 10^{-3}$, $\omega = 800$ (stars). (c) Comparison of the asymptotic prediction of r_0^{opt} obtained by solving (5.12) (solid curve), and results from numerical solutions of (1.15) with $\varepsilon = 1 \times 10^{-3}$ (circles) and $\varepsilon = 5 \times 10^{-3}$ (stars). Here, $\omega_0 = \varepsilon\omega$.

The leading order far-field behavior of μ in (5.2) must be independent of the geometry of Ω_1 so that in the far field, μ must be a constant multiple of $F = K_0(s_0|\boldsymbol{\xi}|/2)e^{-s_0\eta/2}$, which satisfies (5.2) in the case where Ω_1 is the contour on which $F = -1$. Then, for the internal parabolic layer of extent $\mathcal{O}(\sqrt{\varepsilon})$, we introduce the rescaled variables $\hat{r} = \sqrt{\omega_0}(r - r_0)/\sqrt{\varepsilon}$ and $\hat{\theta} = 2\pi - \theta$ and follow the analysis of §4 to obtain from (1.15a)

$$u_{\hat{r}\hat{r}} - u_{\hat{\theta}} = 0\,, \qquad u(\hat{r},0) = \sqrt{\varepsilon}c\delta(\hat{r}) + u_0\,, \tag{5.8}$$

where c is an $\mathcal{O}(1)$ constant and u_0 is given by (5.3). The solution in the internal layer then follows directly from (4.13). As discussed in §4, the only term in the inner and internal layers relevant to the leading order expression for $M(r_0;\omega)$ is the constant term u_0, which is required to uniquely determine the leading order outer solution.

For the outer equation with $\omega = \omega_0/\varepsilon$ in (1.15a), the leading order behavior of the solution must be radially symmetric. With the matching condition $u = u_0$ on the ring $r = r_0$, we therefore obtain the radially symmetric problem

$$u_{rr} + \frac{1}{r}u_r + 1 = 0\,, \quad \mathbf{x} \in \Omega \setminus \{\mathbf{x} : |\mathbf{x}| = r_0\}\,; \tag{5.9a}$$

$$u_r = 0\,, \quad \mathbf{x} \in \partial\Omega\,; \qquad u \text{ bounded as } r \to 0\,; \quad u = u_0\,, \quad |\mathbf{x}| = r_0\,, \tag{5.9b}$$

with u_0 determined empirically from Figure 11(a). The dependence of u on ω_0 is through that of u_0 on $s_0 = r_0\omega_0$. The solution to (5.9) is

$$u(r) = \frac{r_0^2 - r^2}{4} + u_0(s_0) + \frac{1}{2}\Theta(r - r_0)\log\left(\frac{r}{r_0}\right)\,, \tag{5.10}$$

where $\Theta(r)$ is the Heaviside step function. Integrating u in (5.10) over the domain Ω, the leading order expression for the mass $M(r;\omega)$ may then be written

$$M(r_0;\omega) = M(r_0;\omega_0) = \pi\left[\frac{r_0^2}{2} - \frac{3}{8} - \frac{1}{2}\log(r_0) + u_0(r_0\omega_0)\right]\,; \qquad \omega_0 \equiv \varepsilon\omega\,. \tag{5.11}$$

A comparison of $M(r_0;\omega)$ as given by (5.11) versus numerical results as computed from (1.15) is shown in Figure 11(b) for $\omega_0 = 4$. The solid curve is calculated from (5.11) with u_0 given in Figure 11(a), while the circles and stars are from numerical solutions of (1.15) with $\varepsilon = 2.5 \times 10^{-3}$ and $\varepsilon = 5 \times 10^{-3}$, respectively. The agreement between the circles and stars confirms the analytical result that M is independent of ε for fixed ω_0.

To calculate the optimal radius r_0^{opt}, we set to zero the derivative of $M(r_0;\omega_0)$ in (5.11) with respect to r_0. That is, the optimal radius r_0^{opt} satisfies

$$r_0^{opt} - \frac{1}{2r_0^{opt}} + \omega_0 u'(s_0) = 0\,. \tag{5.12}$$

Solving (5.12) numerically for various ω_0, we obtain the solid curve in Figure 11(c). The circles and stars in Figure 11(c) are results obtained from numerical solutions of (1.15) with $\varepsilon = 1 \times 10^{-3}$ (circles) and $\varepsilon = 5 \times 10^{-3}$ (stars) and $\omega = \omega_0/\varepsilon$. We make several remarks. First, the agreement between the circles and the stars confirms that r_0^{opt} is a function only of the product $\varepsilon\omega \equiv \omega_0$, not ε or ω individually. The size of the trap and the frequency of rotation may then be said to be in balance, as doubling one parameter has the same effect on the optimal radius as halving the other. This is in contrast to the $\omega \sim \mathcal{O}(1)$ regime in which r_0^{opt} depends only on ω and not ε.

Second, the numerical results appear to diverge from the asymptotics for large ω_0. This may be due to the fact that the analysis assumes $\omega = \varepsilon^{-1}\omega_0$ with $\omega_0 = \mathcal{O}(1)$; for $\omega_0 \gg 1$, we observe numerically that r_0^{opt} asymptotes to a value slightly below the line $r_0^{opt} = 1/\sqrt{2}$, as predicted by (2.4). Lastly, we illustrate in Figure 12 the transition from $r_0^{opt} \approx 1$ in the $1 \ll \omega \ll \mathcal{O}(\varepsilon^{-1})$ regime to that shown in Figure 11(c) for the $\omega \sim \mathcal{O}(\varepsilon^{-1})$ regime. Figures 12(a) and 12(b), generated from numerical solutions of (1.15) with $\omega_0 = 1$ (left) and $\omega_0 = 1.5$ (right), each show two local minima in the relationship $M(r_0;\omega_0)$. The minimum located near $r_0 = 1$ is that which has persisted from the $1 \ll \omega \ll \mathcal{O}(\varepsilon^{-1})$ regime, while the one located away from $r_0 = 1$ is formed as ω enters the $\omega \sim \mathcal{O}(\varepsilon^{-1})$ regime. The results in Figure 12 then suggest that the transition occurs at some $\omega_0^{(c)} \in (1, 1.5)$ at which the value of M at the left local minimum dips below that of M at the right minimum. The location of the left minimum continues to decrease in r_0 for increasing ω_0, as illustrated by Figure 11(c). The leading order expression for $M(r_0;\omega)$ in (5.11) does not capture the right minimum, as its derivation relies on an $\mathcal{O}(1)$ distance between the boundaries of the trap and domain.

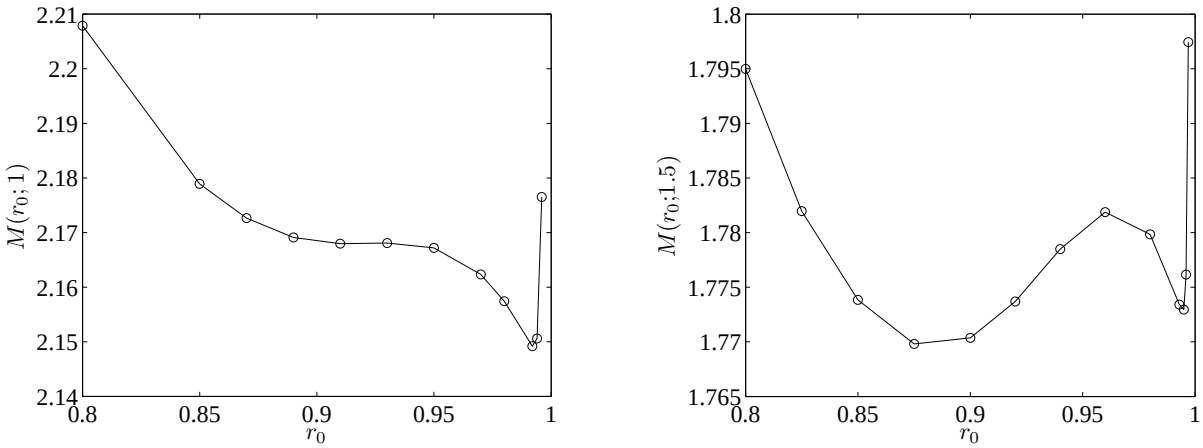

(a) mass versus r_0 with $\omega_0 = 1$

(b) mass versus r_0 with $\omega_0 = 1.5$

Figure 12: The relationship $M(r_0;\omega_0)$, generated from numerical solutions of (1.15) with (a) $\omega_0 = 1$ and (b) $\omega_0 = 1.5$. Here, $\varepsilon = 1 \times 10^{-3}$. In (a), the local minimum away from $r_0 = 1$ is less optimal than that near $r_0 = 1$. In (b), the situation reverses whereby the left local minimum dips below that at the right. The location of the left minimum continues to decrease in r_0 for increasing ω_0, as illustrated by Figure 11(c).

6 Discussion

We have studied the average MFPT over a unit disk domain with a small rotating trap. By taking advantage of the radial geometry, we were able to extend the asymptotic techniques that were developed for stationary traps to the problem of a moving trap. With this radial symmetry, we showed that minimizing the average MFPT was equivalent to minimizing the steady-state mass of a simple diffusive system with uniform feed and a rotating Dirichlet trap.

Several surprising "bifurcations" emerge. For small angular velocities $(0 \leq \omega < \omega_c \approx 3.026)$, the trap should be located at the center of the disk in order to minimize the average MFPT. When ω is large but fixed with $\varepsilon \to 0$ (that

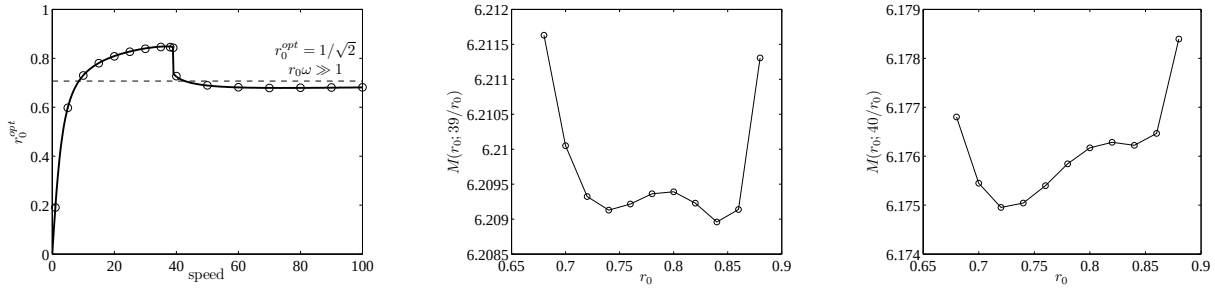

(a) r_0^{opt} versus $r_0\omega$ (b) mass versus r_0 with $r_0\omega = 39$ (c) mass versus r_0 with $r_0\omega = 40$

Figure 13: (a) Asymptotic (solid) and numerical (circles) results for r_0^{opt} for a range of speed $r_0\omega$. Unlike the case with constant ω, no bifurcation is observed so that $r_0^{opt} > 0$ for any $r_0\omega > 0$. The optimal radius reaches a maximum of $r_0^{opt} \approx 0.85$ when $r_0\omega \approx 39$ before a transition occurs to a smaller optimal radius. The transition is illustrated in the mass versus r_0 plots shown in (b) and (c) for $r_0\omega = 39$ and $r_0\omega = 40$, respectively. Two local minima are present. As $r_0\omega$ increases, the left minimum dips below that at the right. The results were obtained from numerical solutions of (1.15) with $\varepsilon = 1 \times 10^{-3}$. The same transition may also be observed from asymptotic results.

is, $1 \ll \omega \ll \mathcal{O}(\varepsilon^{-1})$), the trap should be located very close to the boundary of the disk. On the other hand when ε is small but fixed with $\omega \to \infty$ (that is, $\omega \gg \mathcal{O}(\varepsilon^{-1})$), the optimal trap radius approaches $1/\sqrt{2}$. In this case, the path taken by the trap subdivides the unit disk into two regions of equal area. Because ω is so large, such a regime is equivalent to having a trapping boundary all along the length of the path: that is, from the particle point of view, the trap appears to be simultaneously present all along its path. Most interestingly, there is a discontinuous "jump" in the optimal radius (at around $\omega \approx 10^3$ in Figure 3) as ω is increased. This "jump" occurs due to the presence of two local minima, one of which overtakes the other as ω is increased; see also Figure 12.

The most intricate regime is precisely the transition regime $\omega = \mathcal{O}(\varepsilon^{-1})$ where the "jump" occurs. In §5 we used a boundary integral method approach to compute the asymptotics of the optimal radius in the regime $\omega = \mathcal{O}(\varepsilon^{-1})$. By doing so, we captured the transition between the regime $1 \ll \omega \ll \mathcal{O}(\varepsilon^{-1})$ in which $r_0^{opt} \to 1$, and the regime $\Omega \gg \mathcal{O}(\varepsilon^{-1})$ in which $r_0^{opt} \to 1/\sqrt{2}$.

The moving trap is very closely related to problems involving moving sources for the diffusion equation; see for example [48] and references therein. Some applications include welding [49], calculation of heat flux generated by friction in a pin-on-disc tribometer [50], and welding with CO_2 lasers [48].

Throughout the paper, we considered the problem of computing the optimal radius as a function of angular velocity ω. Equally, it is interesting to see how the optimal radius depends on the *speed* $s = r_0\omega$. This dependence is shown in Figure 13. As with Figure 3, note that the optimal radius approaches $r_0 \sim 1/\sqrt{2}$ for large ω, as well as the presence of the "jump" near $\omega \approx 40$ independent of ε. Two notable differences are that r_0^{opt} does not make an asymptotic approach to 1 for large speed, and there is also no "bifurcation" near the origin: the optimal r_0 is strictly positive regardless of how small s is. Note that the $r_0^{opt} \sim 1/\sqrt{2}$ result in both the $1 \ll \omega \ll \mathcal{O}(\varepsilon^{-1})$ and $\omega \sim \mathcal{O}(\varepsilon^{-1})$ regimes may be inferred from (4.22) and (5.11) by replacing ω and ω_0 by s/r_0 and $\varepsilon s/r_0$, respectively, and differentiating the resulting expression with s held constant. The same result for the $\omega \gg \mathcal{O}(\varepsilon^{-1})$ regime is immediate from (2.3).

Of course, the problem we studied has a very special geometry and it is an open question to consider the obvious generalizations: a non-circular domain, more complex trap motion (with or without a stochastic component), multiple traps, etc. On the other hand, this simple setting allows for a detailed analysis which shows that even a very simple situation has a surprisingly rich structure, with several different transitions depending on the relative strengths of the trap radius ε and its rotation rate ω. As such, it provides a good test case for future studies of MFPT with moving traps.

Acknowledgments

J. C. Tzou was supported by an AARMS Postdoctoral Fellowship. T. Kolokolnikov is supported by NSERC discovery and NSERC accelerator grants. We thank Michael Ward for useful discussions and suggestions.

References

[1] S. Redner, A guide to first-passage processes, Cambridge University Press, 2001.

[2] C. Chevalier, O. Bénichou, B. Meyer, R. Voituriez, First-passage quantities of brownian motion in a bounded domain with multiple targets: a unified approach, Journal of Physics A: Mathematical and Theoretical 44 (2) (2011) 025002.

[3] T. Chou, M. D'Orsogna, First passage problems in biology, pre-print .

[4] A. J. Bray, S. N. Majumdar, G. Schehr, Persistence and first-passage properties in nonequilibrium systems, Advances in Physics 62 (3) (2013) 225–361.

[5] A. Drewitz, J. Gärtner, A. F. Ramírez, R. Sun, Survival probability of a random walk among a Poisson system of moving traps, in: Probability in Complex physical systems, Springer, 2012, pp. 119–158.

[6] Z. Schuss, The narrow escape problems – A short review of recent results, Journal of Scientific Computing 53 (1) (2012) 194–210.

[7] D. Holcman, Z. Schuss, Time scale of diffusion in molecular and cellular biology, Journal of Physics A: Mathematical and Theoretical 47 (17) (2014) 173001.

[8] M. S. Titcombe, M. J. Ward, An asymptotic study of oxygen transport from multiple capillaries to skeletal muscle tissue, SIAM Journal on Applied Mathematics 60 (5) (2000) 1767–1788.

[9] E. Barkai, D. A. Kessler, Transport and the first passage time problem with application to cold atoms in optical traps, arXiv preprint arXiv:1305.0081 .

[10] R. Yvinec, M. R. D'Orsogna, T. Chou, First passage times in homogeneous nucleation and self-assembly, The Journal of chemical physics 137 (24) (2012) 244107.

[11] L. Mirny, M. Slutsky, Z. Wunderlich, A. Tafvizi, J. Leith, A. Kosmrlj, How a protein searches for its site on DNA: the mechanism of facilitated diffusion, Journal of Physics A: Mathematical and Theoretical 42 (43) (2009) 434013.

[12] O. Bénichou, Y. Kafri, M. Sheinman, R. Voituriez, Searching fast for a target on DNA without falling to traps, Physical review letters 103 (13) (2009) 138102.

[13] D. Coombs, R. Straube, M. Ward, Diffusion on a sphere with localized traps: Mean first passage time, eigenvalue asymptotics, and Fekete points, SIAM Journal on Applied Mathematics 70 (1) (2009) 302–332.

[14] M. Moreau, G. Oshanin, O. Bénichou, M. Coppey, Pascal principle for diffusion-controlled trapping reactions, Physical Review E 67 (4) (2003) 045104.

[15] G. Oshanin, O. Bénichou, M. Coppey, M. Moreau, Trapping reactions with randomly moving traps: Exact asymptotic results for compact exploration, Physical Review E 66 (6) (2002) 060101.

[16] N. Komarov, P. Winkler, Capturing the drunk robber on a graph, arXiv preprint arXiv:1305.4559 .

[17] G. Oshanin, O. Vasilyev, P. Krapivsky, J. Klafter, Survival of an evasive prey, Proceedings of the National Academy of Sciences 106 (33) (2009) 13696–13701.

[18] A. Gabel, S. N. Majumdar, N. K. Panduranga, S. Redner, Can a lamb reach a haven before being eaten by diffusing lions?, Journal of Statistical Mechanics: Theory and Experiment 2012 (05) (2012) P05011.

[19] A. Kehagias, D. Mitsche, P. Prałat, Cops and invisible robbers: The cost of drunkenness, Theoretical Computer Science 481 (2013) 100–120.

[20] D. Holcman, Z. Schuss, The narrow escape problem, SIAM Review 56 (2) (2014) 213–257.

[21] Z. Schuss, A. Singer, D. Holcman, The narrow escape problem for diffusion in cellular microdomains, Proceedings of the National Academy of Sciences 104 (41) (2007) 16098–16103.

[22] A. Singer, Z. Schuss, D. Holcman, Narrow escape, part ii: The circular disk, Journal of statistical physics 122 (3) (2006) 465–489.

[23] S. Pillay, M. J. Ward, A. Peirce, T. Kolokolnikov, An asymptotic analysis of the mean first passage time for narrow escape problems: Part i: Two-dimensional domains, Multiscale Modeling & Simulation 8 (3) (2010) 803–835.

[24] A. F. Cheviakov, M. J. Ward, R. Straube, An asymptotic analysis of the mean first passage time for narrow escape problems: Part ii: The sphere, Multiscale Modeling & Simulation 8 (3) (2010) 836–870.

[25] T. Kolokolnikov, M. S. Titcombe, M. J. Ward, Optimizing the fundamental Neumann eigenvalue for the Laplacian in a domain with small traps, European Journal of Applied Mathematics 16 (2) (2005) 161–200.

[26] D. Toussaint, F. Wilczek, Particleantiparticle annihilation in diffusive motion, The Journal of Chemical Physics 78 (5).

[27] A. Szabo, R. Zwanzig, N. Agmon, Diffusion-controlled reactions with mobile traps, Physical review letters 61 (21) (1988) 2496.

[28] S. A. Rice, Diffusion-limited reactions, Elsevier, 1985.

[29] M. Bramson, J. L. Lebowitz, Asymptotic behavior of densities in diffusion-dominated annihilation reactions, Physical review letters 61 (21) (1988) 2397.

[30] A. J. Bray, R. A. Blythe, Exact asymptotics for one-dimensional diffusion with mobile traps, Physical review letters 89 (15) (2002) 150601.

[31] O. Bénichou, M. Coppey, M. Moreau, P. Suet, R. Voituriez, Optimal search strategies for hidden targets, Physical review letters 94 (19) (2005) 198101.

[32] T. H. Chung, G. A. Hollinger, V. Isler, Search and pursuit-evasion in mobile robotics, Autonomous Robots 31 (4) (2011) 299–316.

[33] O. Bénichou, R. Voituriez, From first-passage times of random walks in confinement to geometry-controlled kinetics, Physics Reports 539 (4) (2014) 225–284.

[34] L. Giuggioli, S. Pérez-Becker, D. P. Sanders, Encounter times in overlapping domains: Application to epidemic spread in a population of territorial animals, Physical review letters 110 (5) (2013) 058103.

[35] D. Holcman, I. Kupka, The probability of an encounter of two Brownian particles before escape, Journal of Physics A: Mathematical and Theoretical 42 (31) (2009) 315210.

[36] V. Tejedor, O. Bénichou, R. Metzler, R. Voituriez, Residual mean first-passage time for jump processes: theory and applications to lévy flights and fractional brownian motion, Journal of Physics A: Mathematical and Theoretical 44 (25) (2011) 255003.

[37] J. C. Tzou, S. Xie, T. Kolokolnikov, Drunken robber, tipsy cop: First passage times, mobile traps, and hopf bifurcations, arXiv preprint arXiv:1410.1391 .

[38] J. E. Fletcher, S. Havlin, G. H. Weiss, First passage time problems in time-dependent fields, Journal of statistical physics 51 (1-2) (1988) 215–232.

[39] J. J. Brey, J. Casado-Pascual, First passage time problems and resonant behavior on a fluctuating lattice, Physica A: Statistical Mechanics and its Applications 212 (12) (1994) 123 – 131.

[40] J. A. Revelli, C. E. Budde, H. S. Wio, Diffusion in fluctuating media: resonant activation, Physica A: Statistical Mechanics and its Applications 342 (1) (2004) 1–8.

[41] A. K. Dhara, T. Mukhopadhyay, Coherent stochastic resonance in one dimensional diffusion with one reflecting and one absorbing boundaries, Journal of statistical physics 107 (3-4) (2002) 685–703.

[42] B. Dybiec, E. Gudowska-Nowak, Resonant activation in the presence of nonequilibrated baths, Physical Review E 69 (1) (2004) 016105.

[43] A. S. Pikovsky, J. Kurths, Coherence resonance in a noise-driven excitable system, Physical Review Letters 78 (5) (1997) 775.

[44] Flexpde is a general-purpose commercial package to solve pde's, see www.pdesolutions.com .

[45] M. Abramowitz, I. Stegun, Handbook of Mathematical Functions: With Formulas, Graphs, and Mathematical Tables, Applied mathematics series, Dover Publications, 1972.

[46] D. Hahn, M. Ozisik, Heat Conduction, 3rd Edition, John Wiley and Sons, 2012.

[47] J. Choi, D. Margetis, T. M. Squires, M. Z. Bazant, Steady advection–diffusion around finite absorbers in two-dimensional potential flows, Journal of Fluid Mechanics 536 (2005) 155–184.

[48] M. Akbari, D. Sinton, M. Bahrami, Geometrical effects on the temperature distribution in a half-space due to a moving heat source, Journal of Heat Transfer 133 (6) (2011) 064502.

[49] H. Cline, T. Anthony, Heat treating and melting material with a scanning laser or electron beam, Journal of Applied Physics 48 (1977) 3895–3900.

[50] N. Laraqi, N. Alilat, J. de Maria, A. Baïri, Temperature and division of heat in a pin-on-disc frictional device–exact analytical solution, Wear 266 (7) (2009) 765–770.